

# A 3-D Failure Initiation Criterion from a Sharp V-notch Edge in Elastic Brittle Structures

Dedicated to prof. Dominique Leguillon on the occasion of his retirement

Zohar YOSIBASH<sup>a,\*</sup>, Brigit MITTELMAN<sup>a</sup>

<sup>a</sup>*Department of Mechanical Engineering, Ben-Gurion University of the Negev, Beer-Sheva 84105, Israel*

---

## Abstract

A three-dimensional failure initiation criterion in brittle materials containing a sharp V-notch is presented and validated by experiments. It is based on simultaneous fulfilment of the stress requirement and a finite fracture mechanics energy release rate (ERR) requirement.

Since the ERR cannot determine failure initiation direction for dominant mode III loading, the failure initiation orientation is determined solely by stress considerations and the force at fracture is determined by both ERR and stress requirements.

Experiments on PMMA, Graphite and MACOR V-notched specimens loaded by three modes demonstrated that predicted fracture load was mostly within 6.5% (RMS) of experimental values.

---

---

\*Corresponding author

*Email address:* zohary@bgu.ac.il (Zohar YOSIBASH)

## Nomenclature

### General

Symbol	Meaning
$\delta\Pi$	The difference in the potential energy between a V-notched 3D linear elastic domain with and without a small crack
$H_{ij}$	Geometric functions
$\mathcal{G}$	Energy release rate
$\mathcal{G}_c$	Critical energy release rate in mode I
$K_I, K_{II}, K_{III}$	Mode I, II and III stress intensity factors
$K_{Ic}$	Mode I fracture toughness
$F_c$	Failure load of the specimen
$\boldsymbol{\sigma}$	Stress tensor
$\sigma_n$	Stress normal to the rotated plane
$\sigma_{n,avg}$	Average stress normal to the rotated plane
$\sigma_c$	Critical stress
$\alpha_i$	Eigenvalues
$\mathbf{S}_i(\theta^*)$	Eigen-stress associated with the eigenvalue $\alpha_i$
$A_i(z)$	Generalized Edge Stress Intensity Functions
$S$	Crack area
$R$	Outer radius of integration
$h$	V-notch height (depth)
$\gamma$	V-notch inclination angle in relation to the side faces
$\omega$	V-notch solid angle (complementary to $2\pi$ with the notch opening angle)
$E$	Young's modulus
$\nu$	Poisson's ratio
$\alpha$	Counter clockwise rotation angle around the y axis (from the yz reference plane which is the V-notch bisector)
$\theta^*$	Counter clockwise rotation angle around the z axis (from the yz reference plane which is the V-notch bisector)/ an angle measured from the V-notch bisector so that $-\frac{\omega}{2} \leq \theta^* \leq \frac{\omega}{2}$

### Coordinate systems

$(r, \theta^*, z)$	Cylindrical coordinates, the $z$ axis coincides with the V-notch edge and $\theta^*$ is measured from the bisector plane
$\alpha, \theta^*$	Failure initiation rotation angles around V-notch bisector plane
$r_p, \theta_p$	Polar coordinate system in the plane rotated by $\alpha, \theta^*$ around bisector plane
$\theta_{p1}, \theta_{p2}$	Integration limits on the circular sector in the rotated plane

## 1. Introduction

The theory of linear elastic fracture mechanics, in the context of finite fracture mechanics (FFM), was successfully applied in the past fifteen years to predict the onset of fracture at V-notch tips of two dimensional (2-D) domains. Different criteria have been suggested that predict the critical load and fracture initiation angle at the V-notch tip under mode I or mixed mode (I+II) state of stress in brittle elastic materials. These include: the generalized strain energy density (SED) criterion [1, 2, 3, 4], the Novozhilov-Seweryn criterion (stress-based) [5], the sharp V-notch maximum tangential stress (SV-MTS) [6], and the extension of the Leguillon's FFM criterion [7] to plane mixed modes [8, 9, 10, 11, 12, 13]. Leguillon's criterion [7] and its extended formulation for in-plane mixed mode loading [8] are based on the stress and energy release rate requirements (in the framework of FFM) that must be simultaneously satisfied for a virtual finite crack formation at the instance of failure initiation (in [11, 12, 13], the pointwise stress requirement was replaced by an average stress requirement). The criterion for in-plane mixed mode [8] was shown to provide good predictions for crack initiation angle and failure load compared to experimental observations (prediction error under 20%) [9, 14, 15] for a wide range of V-notch angles  $\omega$  ( $280^\circ \leq \omega \leq 340^\circ$ ) and in-plane mode mixity ratios (between 0 and 3.5). This criterion was extended and applied for failure initiation and crack growth along a fiber-matrix interface [16].

However, realistic three dimensional (3-D) structures containing a V-notch may be subject to 3-D mixed mode loading and thus the failure that initiates at the V-notch edge is a much more complex phenomenon compared to the 2-D situation: a) It may initiate at one point along the V-notch edge, or along a set of points instantly, b) The failure surface, at the initiation instance, may be inclined to the bi-sector of the V-notch edge at any spatial angle.

Therefore, a failure initiation criterion in 3-D is not well established. As an illustrative example, one may notice the complex fracture pattern in the rectangular bars with an inclined V-notch subjected to a four point bending shown in Figure 1. The fracture front seems to be

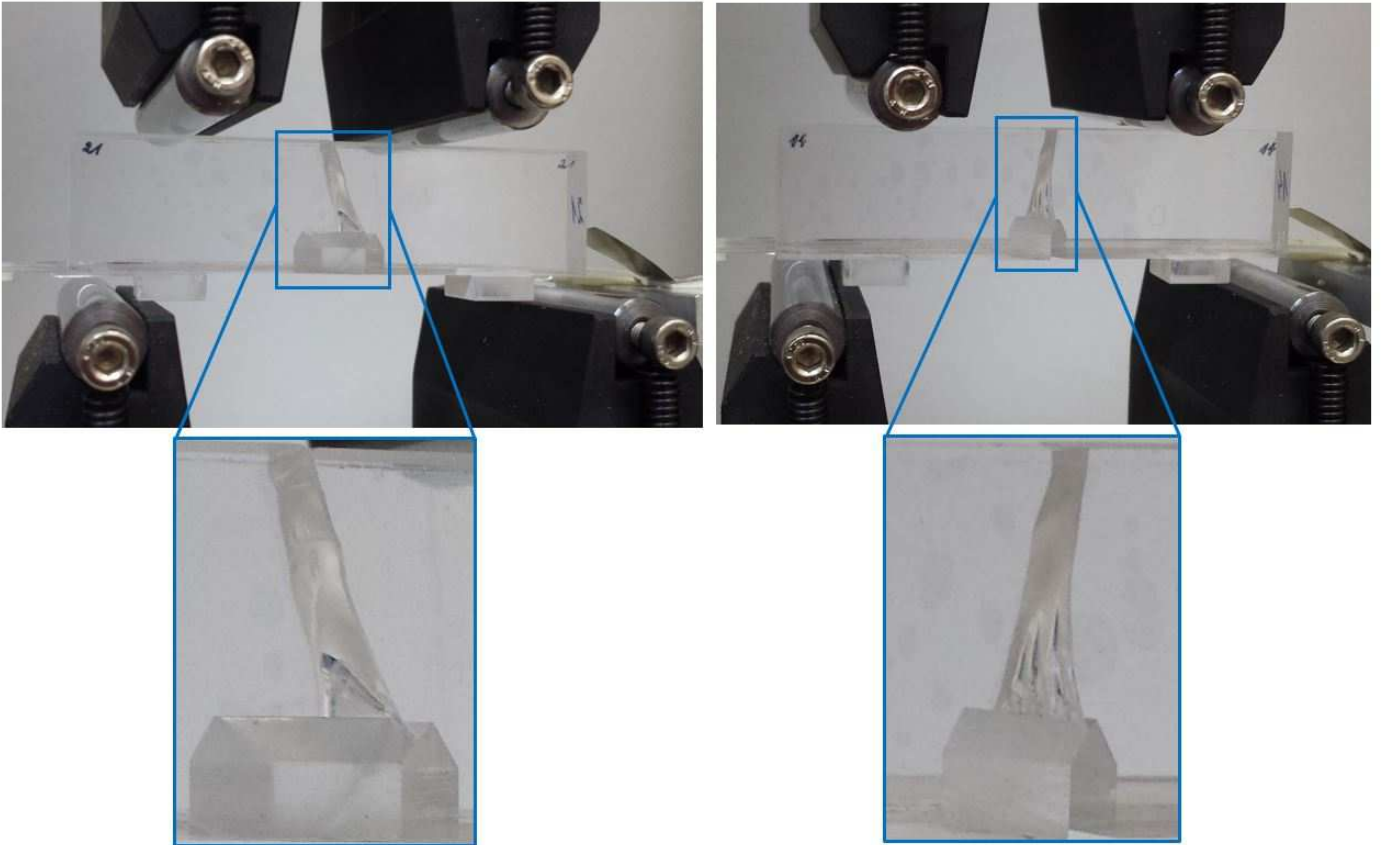


Figure 1: Fracture at the tip of two inclined V-notches (one at  $45^\circ$  (left) and the other at  $30^\circ$  (right)) in PMMA bars under four point bending.

confined at a finite length of the V-notch edge, and fragment immediately as soon as mode III loading is present. We herein focus on the extension of the 2-D failure criterion in [8] to a 3-D state, in an attempt to allow an accurate prediction of the load to fracture and the fracture initiation angle at the V-notch edge under a mixed mode I+II+III condition.

Any failure criterion for a V-notched configuration should reduce to a known failure criterion for the well known crack configuration for  $\omega = 2\pi$ . For 3-D *cracks* there are several failure criteria based on an energy considerations such as the generalized minimum strain

energy density criterion (MSED) [17, 18] (extended from [19]), the generalized maximum energy release rate criterion (MERR) and its variation [17] and maximum mean value of the energy release rate [20, 21, 22]. Most of reported experiments address in-plane mixed mode (I+II) (such as [23, 24, 19, 25]) and show good correlation with the failure criteria (MSED, MERR, MNSC) as long as the mode mixity is small (mode II is relatively weak compared to mode I, or  $\frac{K_{II}}{K_I} \lesssim 0.5$ ).

Failure criteria for cracks based on a stress approach include the maximum normal stress criterion (MNSC) [26, 27], the maximum principal stress criterion (MPSC) [28], maximum mean value of  $K_I$  criterion [20] and the generalized empirical elliptic criterion [17].

It is important to realize that most of the failure initiation criteria in 3-D domains proposed for a *crack* configuration under a general mixed mode loading (I+II+III) involve assumptions that limit their ability to describe a general state of crack initiation. For example, most past failure initiation criteria consider one failure initiation angle (which means that  $K_{III}$  affects only the fracture load but not the fracture direction), and/or disregard the dependence of the stress intensity factor  $K_{III}$  on the coordinate along the crack edge [17, 26, 28, 27, 18]. Therefore, these criteria are not appropriate for three-mode loading conditions. In Lazarus et al. [20] a mesoscopically segmented fracture surface was represented by a macroscopic smoothly twisting crack extension. Mixed mode I+III was considered and extensively discussed in Lin et. al [29] and Pham et. al [30]. Lin et al. [29] proposed an initiation criterion which is a generalization of an Irwin-type criterion, and states that the crack initiates from an existing crack in a direction where both mode II and III SIFs vanish ( $K_{II} = K_{III} = 0$ ), and mode I stress intensity factor (SIF) equals  $K_{IC}$ . In this criterion, the faceted crack front is characterized by a single angle of fragmentation (a “factory roof” profile), so it addresses a special case. This special case is further discussed and examined in [30]. It is worth mentioning here that some recent works emphasize the role of a coupled mode II and III state of stress in failure initiation criteria at 3D cracks [31].

The experiments used to validate the aforementioned criteria are also limited. Experiments conducted on PMMA and brittle steels which involved mode III loading conditions [18] showed tens of percent of deviation between values of the fracture envelope ( $\frac{K_{III}}{K_{IC}}$  as a function of  $\frac{K_I}{K_{IC}}$ ) for mode I+III loading conditions as predicted by the minimum strain

energy density (MSED) [17, 18] and the maximum energy release rate (MERR) [17] criteria, and experimental results (see also [32]). In [26, 27] the maximum normal stress criterion (MNSC) showed tens of percent of deviation in fracture initiation angle values compared to experimental results. The maximum principal stress criterion (MPSC) [28] also shows poor correlation with experimental findings – up to 80% error in determining the fracture angle in the presence of mode III [20]. The mean energy release rate criterion is closer to the experimental results, showing up to 35% deviation and the mean  $K_I$  criterion showed up to 20% deviation compared to the same experiments [20].

We herein generalize the 2-D (in-plane loading) failure initiation criterion from sharp V-notches by Yosibash et al. (modes I+II) [8], and Leguillon (mode I) [7] to a 3-D setting, and validate it by experimental observations in three different brittle elastic specimens. The criterion is based on a *virtual* planar circular sector crack at the V-notch edge whose dimension and orientation simultaneously fulfill the stress criterion and finite fracture mechanics energy release rate criterion.

Preliminaries and notations, including the stress tensor in the vicinity of a 3-D V-notch edge are provided in section 2. The finite fracture mechanics energy release rate (ERR) in 3-D in the context of finite fracture mechanics is introduced next in section 3. It is computed by the difference in potential energy between a domain with a V-notch and same domain with a small circular sector flat crack created along the V-notch edge in an arbitrary direction. This ERR is provided as an asymptotic series (see [33]), necessary due to the amount of required calculations. The stress criterion in 3-D is discussed in section 4, followed by the explicit formulation of the failure criterion in section 5. This criterion is based on the determination of a virtual planar circular-sector shaped crack whose orientation is chosen to satisfy the stress criterion, and its area is determined so to simultaneously satisfy the stress and ERR criteria. Once this virtual crack is determined, the critical load is known. To validate the failure criterion, we performed experiments detailed in section 6. V-notched specimens made of Poly-Methyl-Methacrylate (PMMA), Graphite and a machinable ceramic (Macor) were loaded to fracture under a mixed mode loading. Failure load and failure initiation angles were measured and compared to the predicted failure load and crack initiation angles in

section 7. We conclude by a summary in section 8.

## 2. Preliminaries and notations

Consider a linear elastic and isotropic 3-D domain having a sharp V-notch with a straight edge and traction free boundary conditions on its surfaces  $\Gamma_1, \Gamma_2$ , Fig. 2. The elastic solution in the vicinity of the V-notch edge is expressed in cylindrical coordinates  $(r, \theta^*, z)$ .  $\theta^* = 0$  along the the  $y$  axis so that  $-\frac{\omega}{2} \leq \theta^* \leq \frac{\omega}{2}$ , and  $z$  axis coincides with the edge ( $yz$  is the V-notch bisector plane).

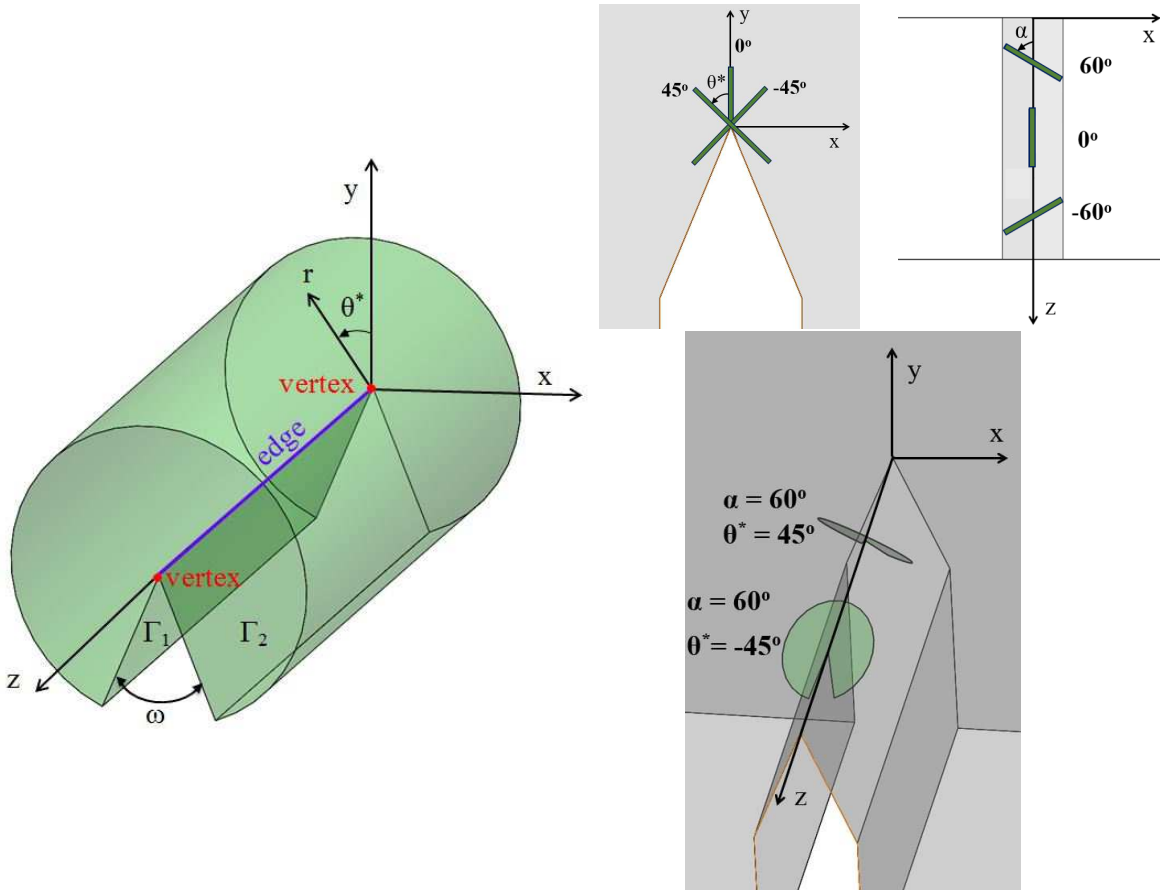


Figure 2: Left: Edge and vertex in a 3-D domain. Right: The definitions of the virtual crack orientation.

The stress field in the vicinity of the singular edge is given by an asymptotic expansion

[33]:

$$\begin{aligned}
\boldsymbol{\sigma}(r, \theta^*, z) &= (\sigma_{rr} \ \sigma_{\theta^*\theta^*} \ \sigma_{zz} \ \sigma_{r\theta^*} \ \sigma_{rz} \ \sigma_{\theta^*z})^T \tag{1} \\
&= A_1(z) \cdot r^{\alpha_1-1} \left\{ \begin{array}{l} \left[ \cos[(1+\alpha_1)\theta^*] + \frac{(3-\alpha_1)}{(1-\alpha_1)} \cdot \frac{\sin[\omega(1+\alpha_1)/2]}{\sin[\omega(1-\alpha_1)/2]} \cdot \cos[(1-\alpha_1)\theta^*] \right] / \sigma_{\theta^*\theta^*}^{(1)}(\theta^*=0) \\ \left[ -\cos[(1+\alpha_1)\theta^*] + \frac{(1+\alpha_1)}{(1-\alpha_1)} \cdot \frac{\sin[\omega(1+\alpha_1)/2]}{\sin[\omega(1-\alpha_1)/2]} \cdot \cos[(1-\alpha_1)\theta^*] \right] / \sigma_{\theta^*\theta^*}^{(1)}(\theta^*=0) \\ \frac{2\lambda}{\lambda+\mu} \cdot \frac{\sin[\omega(1+\alpha_1)/2]}{\sin[\omega(1-\alpha_1)/2]} \cdot \frac{\cos[(1-\alpha_1)\theta^*]}{1-\alpha_1} / \sigma_{\theta^*\theta^*}^{(1)}(\theta^*=0) \\ \left[ -\sin[(1+\alpha_1)\theta^*] + \frac{\sin[\omega(1+\alpha_1)/2]}{\sin[\omega(1-\alpha_1)/2]} \cdot \sin[(1-\alpha_1)\theta^*] \right] / \sigma_{\theta^*\theta^*}^{(1)}(\theta^*=0) \\ 0 \\ 0 \end{array} \right\} \\
&+ A_2(z) \cdot r^{\alpha_2-1} \left\{ \begin{array}{l} \left[ \sin[(1+\alpha_2)\theta^*] + \frac{(3-\alpha_2)}{(1+\alpha_2)} \cdot \frac{\sin[\omega(1+\alpha_2)/2]}{\sin[\omega(1-\alpha_2)/2]} \cdot \sin[(1-\alpha_2)\theta^*] \right] / \sigma_{r\theta^*}^{(2)}(\theta^*=0) \\ \left[ -\sin[(1+\alpha_2)\theta^*] + \frac{\sin[\omega(1+\alpha_2)/2]}{\sin[\omega(1-\alpha_2)/2]} \cdot \sin[(1-\alpha_2)\theta^*] \right] / \sigma_{r\theta^*}^{(2)}(\theta^*=0) \\ \frac{2\lambda}{\lambda+\mu} \cdot \frac{\sin[\omega(1+\alpha_2)/2]}{\sin[\omega(1-\alpha_2)/2]} \cdot \frac{\sin[(1-\alpha_2)\theta^*]}{1+\alpha_2} / \sigma_{r\theta^*}^{(2)}(\theta^*=0) \\ \left[ \cos[(1+\alpha_2)\theta^*] - \frac{(1-\alpha_2)}{(1+\alpha_2)} \cdot \frac{\sin[\omega(1+\alpha_2)/2]}{\sin[\omega(1-\alpha_2)/2]} \cdot \cos[(1-\alpha_2)\theta^*] \right] / \sigma_{r\theta^*}^{(2)} \tilde{\sigma}_{r\theta^*}^{II}(\theta^*=0) \\ 0 \\ 0 \end{array} \right\} \\
&+ A_3(z) \cdot r^{\alpha_3-1} \left\{ \begin{array}{l} 0 \\ 0 \\ 0 \\ 0 \\ \sin\left[\frac{\pi}{\omega}\theta^*\right] \\ \cos\left[\frac{\pi}{\omega}\theta^*\right] \end{array} \right\} + O(r^0)
\end{aligned}$$

where  $A_i(z)$  are the generalized edge stress intensity functions (GESIFs) representing the strength of each singularity and may be computed by the quasi-dual function method [34] and  $\alpha_i$  are the 2-D eigenvalues ( $\alpha_1 = 0.5050097$ ,  $\alpha_2 = 0.6597016$ , for a solid angle of  $\omega = 315^\circ$ ).  $\alpha_3$  is obtained by solving the Laplace equation  $\left(\alpha_3^2 + \frac{\partial^2}{\partial(\theta^*)^2}\right) s_z(\theta^*) = 0$  with homogeneous Neumann boundary conditions. For  $\omega = 315^\circ$ ,  $\alpha_3 = \frac{4}{7}$ .  $\sigma_{\theta^*\theta^*}^{(1)}(\theta^*=0) = \frac{(1+\alpha_1)}{(1-\alpha_1)} \cdot \frac{\sin[\omega(1+\alpha_1)/2]}{\sin[\omega(1-\alpha_1)/2]} - 1$ , and  $\sigma_{r\theta^*}^{(2)}(\theta^*=0) = 1 - \frac{(1-\alpha_2)}{(1+\alpha_2)} \cdot \frac{\sin[\omega(1+\alpha_2)/2]}{\sin[\omega(1-\alpha_2)/2]}$  are normalization factors for the stresses so that for mode I  $\sigma_{\theta^*\theta^*}^{(1)}(\theta^*=0) = 1$  and for mode II  $\sigma_{r\theta^*}^{(2)}(\theta^*=0) = 1$ .  $\lambda, \mu$  are the Lamé constants that may be expressed in terms of the Young modulus  $E$  and the Poisson ratio  $\nu$ .

**Remark 1.** *The angle  $\theta^*$  is more convenient for use because of its symmetry with respect to the V-notch bisector plane. In [33] we have used  $\theta = \theta^* + \frac{\pi}{2}$  and in [35] the angle  $\theta^*$  was denoted by  $\beta$ .*



To determine a spatial orientation of a virtual crack we use in 3-D two angles. These are chosen relative to the V-notch bi-sector plane at the point of crack origin ( $yz$  plane in Fig. 2). The angle  $\alpha$  is a counter-clockwise rotation around  $y$  axis, and  $\theta^*$  is counter-clockwise rotation around  $z$  axis. Since the rotation by  $\alpha$  and  $\theta^*$  is not commutative, we define the rotation starting from the reference plane  $yz$ , first by  $\theta^*$  and then by  $\alpha$ . In Cartesian coordinates the normal to  $yz$  plane is  $(100)$ . The unit normal to each crack orientation plane can be represented in Cartesian or Cylindrical coordinates as follows:

$$\begin{aligned} \begin{pmatrix} n_x \\ n_y \\ n_z \end{pmatrix} &= \begin{pmatrix} \cos \alpha & 0 & \sin \alpha \\ 0 & 1 & 0 \\ -\sin \alpha & 0 & \cos \alpha \end{pmatrix} \begin{pmatrix} \cos \theta^* & -\sin \theta^* & 0 \\ \sin \theta^* & \cos \theta^* & 0 \\ 0 & 0 & 1 \end{pmatrix} \begin{pmatrix} 1 \\ 0 \\ 0 \end{pmatrix} \\ \begin{pmatrix} n_r \\ n_{\theta^*} \\ n_z \end{pmatrix} &= \begin{pmatrix} -\sin \theta^* & \cos \theta^* & 0 \\ -\cos \theta^* & -\sin \theta^* & 0 \\ 0 & 0 & 1 \end{pmatrix} \begin{pmatrix} n_x \\ n_y \\ n_z \end{pmatrix} \\ &= \begin{pmatrix} -\sin \theta^* & \cos \theta^* & 0 \\ -\cos \theta^* & -\sin \theta^* & 0 \\ 0 & 0 & 1 \end{pmatrix} \begin{pmatrix} \cos \alpha & 0 & \sin \alpha \\ 0 & 1 & 0 \\ -\sin \alpha & 0 & \cos \alpha \end{pmatrix} \begin{pmatrix} \cos \theta^* & -\sin \theta^* & 0 \\ \sin \theta^* & \cos \theta^* & 0 \\ 0 & 0 & 1 \end{pmatrix} \begin{pmatrix} 1 \\ 0 \\ 0 \end{pmatrix} \\ &= \begin{pmatrix} \cos \theta^* \sin \theta^* - \cos \alpha \cos \theta^* \sin \theta^* \\ -\cos \alpha \cos^2 \theta^* - \sin^2 \theta^* \\ -\cos \theta^* \sin \alpha \end{pmatrix} \quad (2) \end{aligned}$$

For examples, see [35] (where  $\beta \equiv \theta^*$ ).

### 3. Generalization of the energy release rate (ERR) to 3-D

Because the failure criterion developed is based on a virtual finite crack satisfying simultaneously the strength and ERR requirements it is required to determine in 3-D a crack (assumed to be planar) so that:

1. The crack initiates along a direction at which the energy release rate is maximal, and reaches its critical value:  $-\frac{\delta \Pi}{S} \geq \mathcal{G}_c$ .  $\delta \Pi$  denotes the difference in the potential energy between a V-notched cracked domain and the V-notched un-cracked domain, and  $S$  is the area of the virtual crack.

2. The average normal stress ahead of the V-notch edge within the virtual planar crack surface is larger than a critical value:  $\sigma_{n,avg} \geq \sigma_c$ .

Experiments on 3-D specimens with an inclined V-notch (see Sec 6) show that failure initiation origins may change with the inclination angle, so that crack initiation can be either from a single origin or from several separated origins distributed along the edge. The new criterion should, therefore, be able to describe pointwise, segmented, or continuous fracture. Hence, the new failure criterion must be applied at every point along the V-notch edge, producing different results for fracture initiation angles ( $\alpha, \theta^*$  - enabling a spatial crack initiation) and forces at fracture (associated with the GESIF  $A_I(z)$ ). The smallest force is the failure load.

The expression for  $\delta\Pi$  was explicitly provided by an asymptotic series in [33].  $\delta\Pi$  can be computed for any crack orientation ( $\alpha, \theta^*$ ) and location along the V-notch edge ( $z$ ) by:

$$\begin{aligned}
-\delta\Pi^{Approx} = & A_1^2 \times (\sqrt{S})^{2\alpha_1+1} H_{11}(\alpha, \theta^*) + A_1 A_2 \times (\sqrt{S})^{\alpha_1+\alpha_2+1} \left( H_{12}(\alpha, \theta^*) + H_{21}(\alpha, \theta^*) \right) \\
& + A_2^2 \times (\sqrt{S})^{2\alpha_2+1} H_{22}(\alpha, \theta^*) + A_1 A_3 \times (\sqrt{S})^{\alpha_1+\alpha_3+1} \times \left( H_{13}(\alpha, \theta^*) + H_{31}(\alpha, \theta^*) \right) \\
& + A_2 A_3 \times (\sqrt{S})^{\alpha_2+\alpha_3+1} \left( H_{23}(\alpha, \theta^*) + H_{32}(\alpha, \theta^*) \right) + A_3^2 \times (\sqrt{S})^{2\alpha_3+1} H_{33}(\alpha, \theta^*) + H.O.T.,
\end{aligned} \tag{3}$$

or in concise form:

$$\boxed{-\delta\Pi^{Approx} \approx \sum_{i=1}^3 \sum_{j=1}^3 A_i(z) A_j(z) (\sqrt{S})^{\alpha_i+\alpha_j+1} H_{ij}(\alpha, \theta^*)} \tag{4}$$

where  $S$  is the area of the virtual crack,  $A_i(z)$  are the GESIFs of a V-notch *without* a crack, and the geometrical functions  $H_{ij}$  can be pre-computed and tabulated. Such asymptotic expression substantially reduces the amount of needed calculations, since once  $H_{ij}$  and the GESIFs  $A_i(z)$  are available,  $\delta\Pi$  can be easily computed for any (small) crack area  $S$ , at any location along the V-notch edge  $z$ , and for every crack orientation.

The functions  $H_{ij}$  depend on crack orientation ( $\alpha, \theta^*$ ), material properties ( $E, \nu$ ) and crack shape. The explicit expressions for  $H_{ij}$  are presented herein for *circular cracks*, a V-notch opening angle of  $45^\circ$  ( $\omega = 315^\circ$ ), and for a wide range of material properties. The GESIFs  $A_i(z)$  corresponding to the geometries used in the experiments (Sec. 6) are provided in Sec. 4.

### 3.1. $H_{ij}$ 's for circular cracks

Functions  $H_{ij}(\alpha, \theta^*)$  are detailed in [33]. For discrete values of  $\alpha, \theta^*$  in the range  $-61^\circ \leq \alpha \leq 61^\circ$  and  $-45^\circ \leq \theta^* \leq 45^\circ$  the values of  $H_{ij}$  were computed for a planar virtual crack of circular shape (crack center coincides with the V-notch edge), for a V-notch angle  $\omega = 315^\circ$  and PMMA material properties  $E = 3900 [MPa]$ ,  $\nu = 0.332$  (tabulated data is available in [36]). These discrete values are shown in red dots in Fig. 3. Smooth functions can be then determined to match the discrete values computed.

$H_{ij}$  functions have the following characteristics:

1.  $H_{ij} \approx H_{ji}$  for  $i \neq j$  (mostly less than 1% difference between  $H_{ij}$  and  $H_{ji}$  values).  
 $H_{12}, H_{13}$  and  $H_{23}$  in Fig. 3 represent their counterparts.
2. All  $H_{ij}$  functions show symmetry/anti-symmetry relations with respect to the spatial angles  $\alpha$  and  $\theta^*$ .  $H_{ii}$  are always positive and symmetric in relation to both  $\alpha$  and  $\theta^*$ , while  $H_{12}, H_{21}$  are symmetric with respect to  $\alpha$  and anti-symmetric with respect to  $\theta^*$ ,  $H_{13}, H_{31}$  are symmetric with respect to  $\theta^*$  and anti-symmetric with respect to  $\alpha$ , and  $H_{23}, H_{32}$  are anti-symmetric in relation to both  $\alpha$  and  $\theta^*$ .
3.  $H_{ij}$  have units of  $\frac{mm^2}{N}$ , as can be derived from (4).

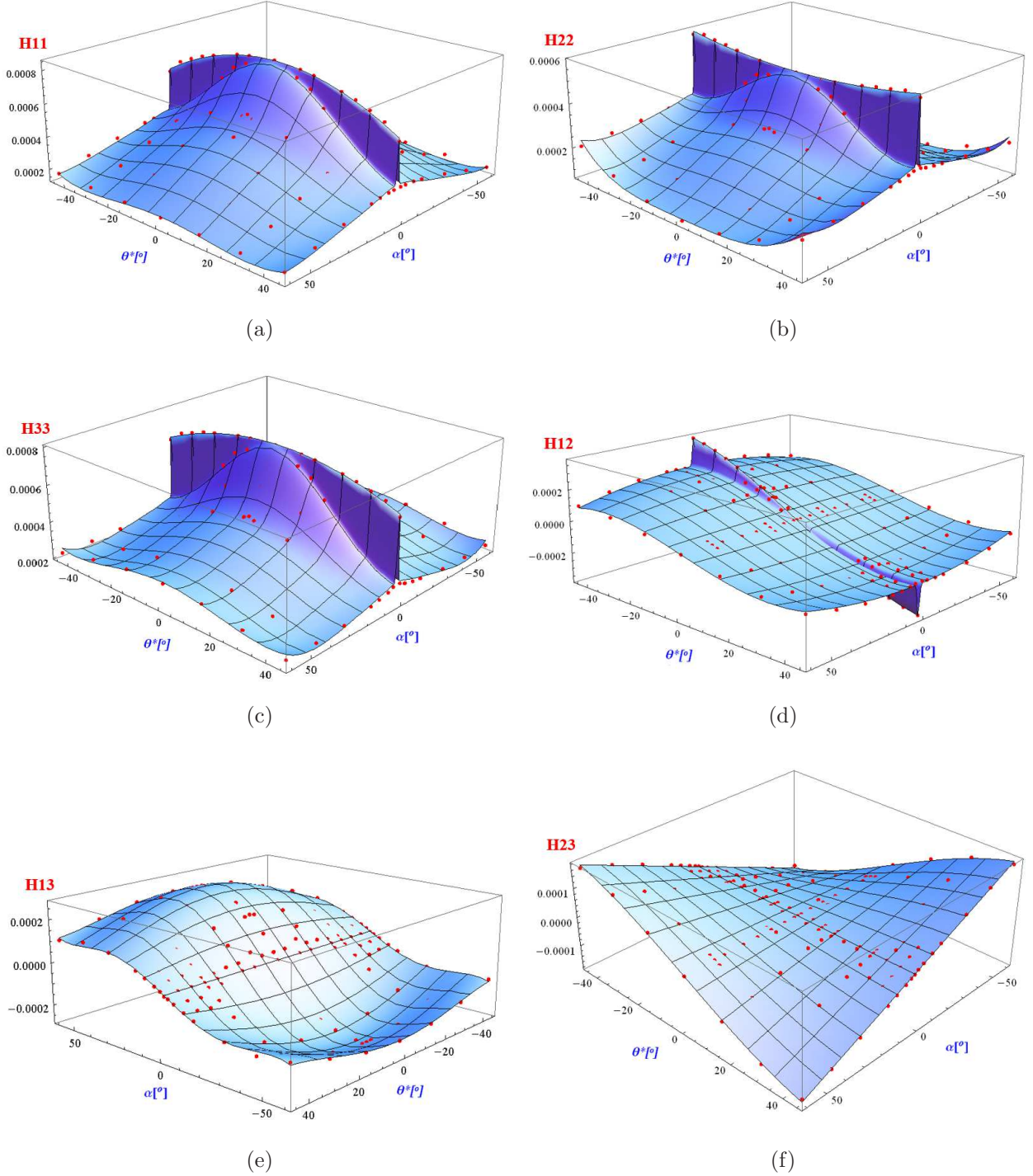


Figure 3:  $H_{ij}$  surfaces for  $E = 3900 \text{ MPa}$ ,  $\nu = 0.332$ ,  $\omega = 315^\circ$  and circular crack shape: (a)  $H_{11}$ , (b)  $H_{22}$ , (c)  $H_{33}$ , (d)  $H_{12} = H_{21}$ , (e)  $H_{13} = H_{31}$  (notice that the axes are inverted to obtain a clear view), (f)  $H_{23} = H_{32}$

In Fig. 3 one can observe a step change at  $\alpha \sim 0$  for most of the  $H_{ij}$  functions. The

steep transition indicates that orientations for which  $\alpha \sim 0$  are more favorable energetically in cases of pure modes (where  $H_{ii}$  define  $\delta\Pi$ ). Also, since angle  $\theta^*$  was defined as in 2-D (rotation angle around the  $z$  axis) it is easy to see that the general trend of  $H_{ij}$  at  $\alpha = 0$  resembles the 2-D behavior, as expected (see [8]).

### 3.1.1. $H_{ij}$ dependence on material properties

In 2-D, the  $H_{ij}$  functions for a new  $E^{new}$  MPa and a new  $\nu^{new}$  can be computed once it is available for a given  $E$  and  $\nu$  according to [8]:

$$H_{ij}^{new}(\omega, \theta^*) = H_{ij}(\omega, \theta^*) \frac{E}{1 - \nu^2} \frac{1 - (\nu^{new})^2}{E^{new}} \quad (5)$$

In 3-D  $H_{ij}$  computations for  $1 \leq E \leq 10^4$  MPa,  $0 \leq \nu \leq 0.4$  show that  $H_{ij}$  depends linearly on  $E$ , but not so for  $\nu$ , so that (5) is incorrect in 3-D. Approximation functions for  $H_{ij}$  are presented in Table 1, where  $E$  and  $\nu$  are parameters (these expressions apply for a V-notch solid angle of  $\omega = 315^\circ$ , and a circular crack shape). Substituting PMMA material properties  $E = 3900$  MPa,  $\nu = 0.332$  approximately reduces to the  $H_{ij}$  expressions in Fig. 3.  $H_{ij}$  values change relatively moderately with  $\nu$ , so when  $\nu$  changes from 0 to 0.4,  $H_{ij}$  changes by approximately 25%, for the same value of  $E$ .

The asymptotic approximation for  $\delta\Pi$  and additional FE methods were used in [35] to examine the energy requirement  $-\frac{\delta\Pi}{S} \geq \mathcal{G}_c$  under loading conditions which involve mode III. According to the energy criterion, the crack initiates along a direction where the ERR is maximum. This was shown to hold true in 2-D (modes I+II [8, 7, 18]), and we examined if it is still so in 3-D (when mode III is present). We have shown [35] that the maximum value of the ERR under dominant mode III loading is always obtained along the V-notch bisector, contrary to experimental observations. Therefore, the energy requirement cannot be used to predict the crack initiation direction in the presence of mode III. In the next section we examine the stress criterion, and address its ability to determine the crack initiation direction under mode III loading.

## 4. Generalization of the stress requirement to 3-D

Since the ERR criterion cannot predict the crack initiation direction in the presence of mode III we consider instead the average normal stress criterion to determine the fail-

$H_{ij}$	Approximation function
$H_{11}$	$\frac{1}{E} \left( \begin{aligned} &2 - 7.1 \cdot 10^{-4}(\theta^*)^2 + \alpha^2(-4.875 \cdot 10^{-4} + 1.1 \cdot 10^{-7}(\theta^*)^2) + 3.51 \cdot 10^{-8}\alpha^4 \\ &+ 1.482 \cdot 10^{-7}(\theta^*)^4 + (1.7238 - 0.8424\nu - 1.6458\nu^2) \exp[-\frac{\alpha^2}{160}] \exp[-\frac{(\theta^*)^2}{1000}] \\ &\quad - 0.0872\nu - 0.2625\nu^2 + 5.915 \cdot 10^{-3}\nu  \alpha  - 3 \cdot 10^{-3}\nu  \theta^*  \\ &+ \left( \begin{aligned} &1.785 + 1.162 \cdot 10^{-4}(\theta^*)^2 - 1.482 \cdot 10^{-7}(\theta^*)^4 +  \theta^*  (-5.785 \cdot 10^{-6} + 0.0164\nu) \\ &\quad - 0.45\nu - 2.577\nu^2 + \exp[-\frac{(\theta^*)^2}{1000}](-1.723 + 0.842\nu + 1.646\nu^2) \end{aligned} \right) \exp[-\frac{\alpha^2}{0.5}] \end{aligned} \right)$
$H_{22}$	$\frac{1}{E} \left( \begin{aligned} &1.221 - 3.67 \cdot 10^{-4}(\theta^*)^2 + \alpha^2(-4.33 \cdot 10^{-4} + 1.08 \cdot 10^{-7}(\theta^*)^2) \\ &\quad + 4.953 \cdot 10^{-8}\alpha^4 + 1.408 \cdot 10^{-7}(\theta^*)^4 - 0.1085\nu - 0.3268\nu^2 \\ &+ (0.667 + 0.928\nu - 0.9516\nu^2) \exp[-\frac{\alpha^2}{90}] \exp[-\frac{(\theta^*)^2}{900}] + 4.141 \cdot 10^{-3}\nu  \alpha  - 3.72 \cdot 10^{-3}\nu  \theta^*  \\ &+ \left( \begin{aligned} &0.694 + 3.67 \cdot 10^{-4}(\theta^*)^2 - 1.409 \cdot 10^{-7}(\theta^*)^4 +  \theta^*  (0.00814 - 0.00773\nu) \\ &\quad + 1.091\nu - 1.341\nu^2 + \exp[-\frac{(\theta^*)^2}{900}](-0.667 - 0.928\nu + 0.952\nu^2) \end{aligned} \right) \exp[-\frac{\alpha^2}{0.5}] \end{aligned} \right)$
$H_{33}$	$\frac{1}{E} \left( \begin{aligned} &1.794 - 6.6 \cdot 10^{-4}(\theta^*)^2 + \alpha^2(-4.173 \cdot 10^{-4} + 5.928 \cdot 10^{-8}(\theta^*)^2) \\ &\quad + 7.644 \cdot 10^{-8}\alpha^4 + 1.51 \cdot 10^{-7}(\theta^*)^4 - 0.133\nu - 0.4\nu^2 \\ &+ (0.9367 + 1.786\nu - 1.626\nu^2) \exp[-\frac{\alpha^2}{75}] \exp[-\frac{(\theta^*)^2}{800}] + 6.22 \cdot 10^{-3}\nu  \alpha  - 3.16 \cdot 10^{-3}\nu  \theta^*  \\ &+ \left( \begin{aligned} &0.981 + 2.88 \cdot 10^{-4}(\theta^*)^2 - 1.51 \cdot 10^{-7}(\theta^*)^4 +  \theta^*  (4.45 \cdot 10^{-3} - 1 \cdot 10^{-4}\nu) \\ &\quad + \nu(1.588 - 0.994\nu) + \exp[-\frac{(\theta^*)^2}{800}](-0.936 - 1.786\nu + 1.626\nu^2) \end{aligned} \right) \exp[-\frac{\alpha^2}{0.5}] \end{aligned} \right)$
$H_{12}(\approx H_{21})$	$\frac{1}{E} \left( \begin{aligned} &3.4 \cdot 10^{-4} + (\theta^*) \cdot (-0.02764 + 2.4 \cdot 10^{-6}\alpha^2 + 0.00165\nu) + (-0.0484 + 0.0019  \alpha )\nu \\ &\quad - 0.146\nu^2 + 5.634 \cdot 10^{-6}(\theta^*)^3 + (-5 \cdot 10^{-4} + 8.28 \cdot 10^{-8}(\theta^*)^2 - 5.634 \cdot 10^{-6}(\theta^*)^3 \\ &\quad + (\theta^*) \cdot (-0.0113 + 0.0123\nu) + 0.0487\nu + 0.1453\nu^2 \exp[-\alpha^2] \end{aligned} \right)$
$H_{13}(\approx H_{31})$	$\frac{1}{E} \left( \begin{aligned} &-6.65 \cdot 10^{-5} + 0.046\alpha - 1.4 \cdot 10^{-5}\alpha^3 - 1.4 \cdot 10^{-5}\alpha(\theta^*)^2 \\ &\quad + 1.41 \cdot 10^{-9}\alpha^5 + 2.43 \cdot 10^{-9}\alpha^3(\theta^*)^2 + 1.056 \cdot 10^{-9}\alpha(\theta^*)^4 \\ &\quad - 7.5 \cdot 10^{-4}\alpha\nu + 0.019\nu - 5.46 \cdot 10^{-4}(\theta^*) \cdot \nu + 0.057\nu^2 \end{aligned} \right)$
$H_{23}(\approx H_{32})$	$\frac{1}{E} \left( \begin{aligned} &-3.18 \cdot 10^{-4}\alpha \cdot \theta^* + 2.863 \cdot 10^{-8}\alpha(\theta^*)^3 - 5.77 \cdot 10^{-4}\alpha\nu \\ &\quad + 0.02235\nu - 6.88 \cdot 10^{-4}\nu \cdot \theta^* + 0.0673\nu^2 \end{aligned} \right)$

Table 1: Approximating functions for  $H_{ij}$  with general material properties ( $\omega = 315^\circ$ , circular crack shape).

ure initiation direction. Failure initiates in a plane to which the average normal stress is maximum.

The failure load needs also to satisfy  $\sigma_n \geq \sigma_c$ , where  $\sigma_n$  is the normal stress to a failure plane, and  $\sigma_c$  is a material property. The closed planar shape of all points at which  $\sigma_n \geq \sigma_c$  determines the virtual crack. Since on each plane the normal stress is different, the virtual crack's shape and area  $S$  depend on orientation, location along the edge  $z$  and the far loading through  $A_i(z)$  (the larger the applied load, the larger is  $S$ ). *To conform with the ERR criterion, instead of a general virtual crack shape, we consider only a circular sector shaped virtual crack.*

The normal stress to a plane determined by (2) is obtained using (1):

$$\begin{aligned}
\sigma_n &= T_i n_i = T_r n_r + T_{\theta^*} n_{\theta^*} + T_z n_z \\
&= \sigma_{rr} n_r^2 + \sigma_{\theta^* \theta^*} n_{\theta^*}^2 + \sigma_{zz} n_z^2 + 2n_r n_{\theta^*} \sigma_{r\theta^*} + 2n_r n_z \sigma_{rz} + 2n_{\theta^*} n_z \sigma_{\theta^* z} \\
&= \sin^4(\alpha/2) \sin^2(2\theta^*) \sigma_{rr}(A_1(z), A_2(z), r, \theta^*) + (\cos(\alpha) \cos^2(\theta^*) + \sin^2(\theta^*))^2 \sigma_{\theta^* \theta^*}(A_1(z), A_2(z), r, \theta^*) \\
&+ \frac{1}{2} (\sin^2(\alpha) + \cos(2\theta^*) \sin^2(\alpha)) \sigma_{zz}(A_1(z), A_2(z), r, \theta^*) \\
&+ \frac{1}{2} (-\sin^2(\alpha) \sin(2\theta^*) + 2\sin^4(\alpha/2) \sin(4\theta^*)) \sigma_{r\theta^*}(A_1(z), A_2(z), r, \theta^*) \\
&- \sin^2(\alpha/2) \sin(\alpha) (\sin(\theta^*) + \sin(3\theta^*)) \sigma_{rz}(A_3(z), r, \theta^*) \\
&+ 2\cos(\theta^*) \sin(\alpha) (\cos(\alpha) \cos^2(\theta^*) + \sin^2(\theta^*))^2 \sigma_{\theta^* z}(A_3(z), r, \theta^*)
\end{aligned} \tag{6}$$

To determine the virtual crack initiation angle we consider the average normal stress in a radial sector of radius R on a plane determined by  $(\alpha, \theta^*)$ :

$$\sigma_{n,avg} \stackrel{\text{def}}{=} \frac{\int_{\theta_{p1}}^{\theta_{p2}} \int_0^R \sigma_n(r_p, \theta_p) r_p dr_p d\theta_p}{\int_{\theta_{p1}}^{\theta_{p2}} \int_0^R r_p dr_p d\theta_p} \tag{7}$$

where  $(r_p, \theta_p)$  are polar coordinates defined in the normal plane. An identical area needs to be considered for all plane orientation so that the normal stress will be comparable. The normal average stress was computed at angles  $(\alpha, \theta^*)$  in intervals of  $2^\circ$  within the range  $-61^\circ \leq \alpha \leq 61^\circ$ ,  $-45^\circ \leq \theta^* \leq 45^\circ$ , and the combination  $(\alpha, \theta^*)$  which resulted in maximum  $\sigma_{n,avg}$  was determined.

Computations were performed by *Mathematica*<sup>1</sup> (code is available for download [37]). Since the integration area is identical for all orientations, the integration limits of  $r_p$  and  $\theta_p$  depend on the normal plane orientation (intersection lines between the V-notch faces and normal plane were computed for each plane). The angle  $\theta_p$  they create in relation to the  $y_p$  axis was calculated as well, these two angles served as the limiting angles in the integration (7). For the integration limiting angles, the upper radial limit of integration R was determined so to obtain a constant area:  $\int_{\theta_{p1}}^{\theta_{p2}} \int_0^R r_p dr_p d\theta_p = \text{const.}$  Computed directions at which  $\sigma_{n,avg}$  is maximum for circular sector areas of 0.1, 0.05, and  $0.03 \text{ mm}^2$ , and pure loading modes (only one  $A_i(z)$  non-zero) are summarized in Table 2.

---

<sup>1</sup>Mathematica is a trademark of Wolfram Research, Inc., Champaign, IL, USA

Integration area $mm^2$	Loading mode	$(\alpha, \theta^*)^\circ$
0.3	I	$(\pm 1, \pm 1)$
	II	$(\pm 1, -45)$
	III	$(41, \pm 1)$
0.2	I	$(\pm 1, \pm 1)$
	II	$(\pm 1, -45)$
	III	$(41, \pm 1)$
0.1	I	$(\pm 1, \pm 1)$
	II	$(\pm 1, -45)$
	III	$(43, \pm 1)$
0.05	I	$(\pm 1, \pm 1)$
	II	$(\pm 1, -45)$
	III	$(41, \pm 1)$

Table 2: Angles at which average maximum normal stress was obtained for pure loading modes (V-notch opening angle  $\omega = 315^\circ$ ).

One may observe that the integration area has a negligible influence on the plane direction at which maximum average normal stress is obtained for mode III, and no influence was observed for modes I and II. We used the area of  $0.1 mm^2$ , which is small compared to specimen dimensions, and is close to the expected orientation for maximum normal stress for mode III. It was confirmed that *the orientation  $(\alpha, \theta^*)$  at which  $\sigma_{n,avg}$  is maximum does not depend on the applied force* (which influences the GESIFs  $A_i(z)$ ). For the same geometry and material properties, the force applied was taken between 1000 N and 4000 N. For each orientation, the value of  $\sigma_{n,avg}$  was increased by the same factor in which the force was increased. Therefore,  $\sigma_{n,avg}$  is calculated for a reference force of 1000 N, and a constant area of  $0.1 mm^2$  for all geometries examined in experiments (see [37]).

The influence of material properties on the failure orientation plane is through the  $\sigma_{zz}$



stress component, which depends on  $\frac{2\lambda}{\lambda+\mu} = 4\nu$ . Since  $\sigma_{zz}$  is the only component of the stress which depends on material properties, the orientation of maximum normal stress is expected to change very moderately with  $\nu$ . Changing  $E$  has no influence on the results.

#### 4.1. Computing the GESIFs $A_i(z)$

For  $\delta\Pi$  and  $\sigma_n$ , one needs the GESIFs  $A_i(z)$  associated with the V-notch edge which are computed by high order finite element models and the quasi-dual-function-method (QDFM) [34], see Fig. 5. For example a FE model of a PMMA specimen tested in experiments is shown in Fig. 4. The polynomial representation of  $A_i(z)$  for all the specimens considered in this paper are presented in Appendix C.

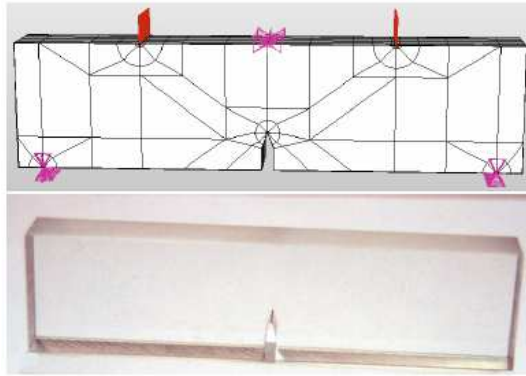


Figure 4: Finite element model of a typical PMMA specimen.

The numerical accuracy of the  $A_i(z)$  computation was assured by performing p-extensions [38] i.e. the polynomial degree of the shape functions in the finite elements was increased from 1 to 8. In addition, the mesh was refined near the notch tip and the loading and clamped regions. The error, measured in the energy norm, was between 0.7% and 3.9% for all models.

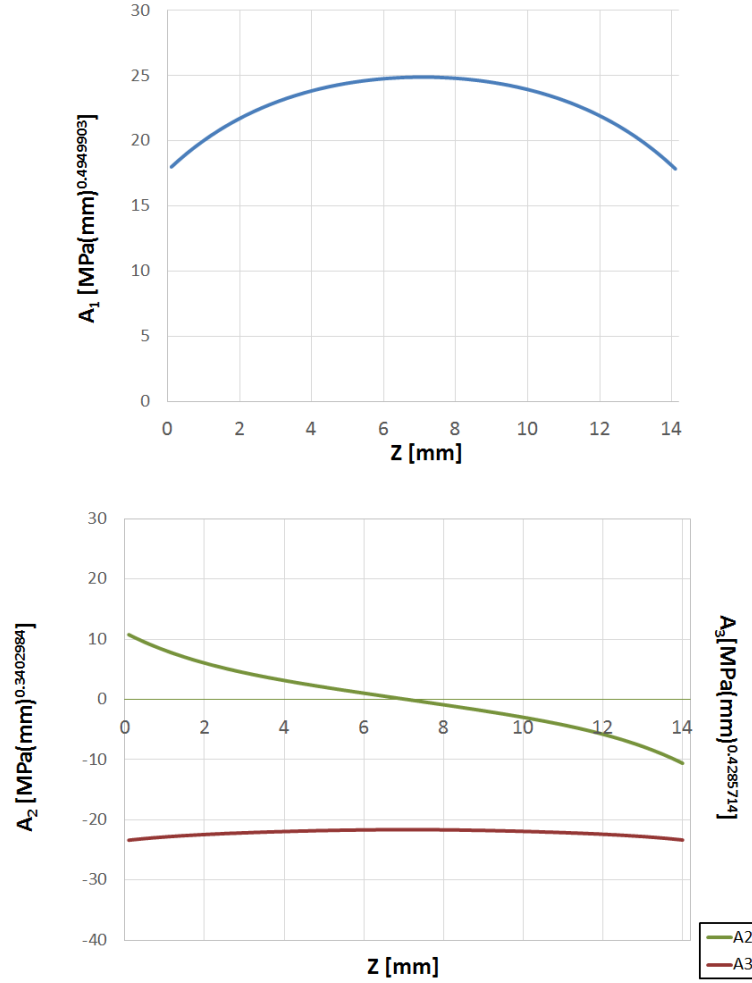


Figure 5: GESIFs in a specimen with the V-notch inclination angle  $\gamma = 45^\circ$  and notch height  $h = 6 \text{ mm}$ , for a force of  $1604 \text{ N}$ .

## 5. The failure initiation criterion in 3-D

Once the failure plane orientation is determined at each point along the V-notch edge, the ERR criterion and the normal stress criterion are used simultaneously to determine the failure load and the virtual crack area.

In the 3-D form of the asymptotic expansion of  $\delta\Pi$  we used circular crack shapes in order to determine  $H_{ij}$  functions. According to the stress criterion, we have shown that the shape of the crack (determined by  $\sigma_n = \sigma_c$  curves) is a more complex “peanut-shape”. If we had used such shapes for  $H_{ij}$ , it would have greatly increased the number and complexity of the required calculations, since this would require finding the specific shape for each orientation.

Because both ERR and stress criteria consider the same virtual crack, for consistency a circular virtual crack shape is assumed in both. The degree of agreement between the predicted and experimental observations will indicate if such an assumption is admissible.

The force at fracture is determined by simultaneously satisfying the ERR and stress requirements:  $-\frac{\delta\Pi}{S} \geq \mathcal{G}_c$  and  $\sigma_{n,avg} \geq \sigma_c$ . The two unknowns  $S$  and  $F_c$  are evaluated at every location  $z$  along the V-notch edge. The minimum force (on of the entire edge) represents the force at fracture.

$$\sigma_{n,avg} = \frac{\int \int \sigma_n(r_p, \theta_p) r_p dr_p d\theta_p}{S} \geq \sigma_c \quad (8)$$

$$\frac{F_c \int \int \tilde{A}_1(z) r^{\alpha_1-1} \mathbf{S}_1(\theta^*) + \tilde{A}_2(z) r^{\alpha_2-1} \mathbf{S}_2(\theta^*) + \tilde{A}_3(z) r^{\alpha_3-1} \mathbf{S}_3(\theta^*) r_p dr_p d\theta_p}{S} \geq \sigma_c$$

$$\begin{aligned} & F_c \left( \tilde{A}_1^2(z) \times (\sqrt{S(F_c)})^{2\alpha_1-1} H_{11}(\alpha, \theta^*) \right. \\ & + \tilde{A}_1(z) \tilde{A}_2(z) \times (\sqrt{S(F_c)})^{\alpha_1+\alpha_2-1} \times (H_{12}(\alpha, \theta^*) + H_{21}(\alpha, \theta^*)) \\ & + \tilde{A}_2^2(z) \times (\sqrt{S(F_c)})^{2\alpha_2-1} H_{22}(\alpha, \theta^*) \\ & + \tilde{A}_1(z) \tilde{A}_3(z) \times (\sqrt{S(F_c)})^{\alpha_1+\alpha_3-1} \times (H_{13}(\alpha, \theta^*) + H_{31}(\alpha, \theta^*)) \\ & + \tilde{A}_2(z) \tilde{A}_3(z) \times (\sqrt{S(F_c)})^{\alpha_2+\alpha_3-1} \times (H_{23}(\alpha, \theta^*) + H_{32}(\alpha, \theta^*)) \\ & \left. + \tilde{A}_3^2(z) \times (\sqrt{S(F_c)})^{2\alpha_3-1} H_{33}(\alpha, \theta^*) \right) \geq \mathcal{G}_c \end{aligned} \quad (9)$$

The area  $S$  depends on the location  $z$ , orientation  $(\alpha, \theta^*)$  and force. The GESIFs  $A_i(F, z)$  is normalized and represented by  $A_i(F, z) = F A_i(1 N, z) = F \tilde{A}_i(z)$ , and  $\tilde{A}_i(z)$  indicates the GESIF for a unit force ( $F = 1 N$ ). Note also that in (8)  $r, \theta^*$  are given as different functions of  $r_p$  and  $\theta_p$ , depending on the considered plane orientation of interest.

The force and area that satisfy simultaneously (8-9) are found numerically by a code written in ‘‘Mathematica’’ [37]. The computational algorithm is briefly explained. Having determined the virtual crack orientation  $(\alpha, \theta^*$  for which  $\sigma_{n,avg}$  is maximum), the input consists of the force ( $F$ ) and edge location ( $z$ ). For every  $z$ , the initial guess for the force is a small number (for example,  $1 N$ ), which then determines the minimum area  $S$  of a circular sector for which the stress criterion (8) is satisfied. Then,  $S$  is substituted in the energy criterion (9) to compute the ERR. Since the initial guess for  $F$  is small, the corresponding ERR is smaller than the critical ERR. The calculation is therefore repeated for a force  $F$  increased by intervals of  $1 N$ , until we obtain the *minimum* force for which ERR reaches its critical value. This calculation is performed for many locations along  $z$ , and for every

geometry and material separately.

To clarify the dependence of the failure load and virtual crack area on the various ingredients of the failure law, we explicitly summarize these herein.

$A_i(z)$  - depend on the general specimen geometry, location  $z$ , and the force  $F$ . Independent of material properties. Defined for a sharp V-notch without a crack and therefore independent of any crack parameters.

$H_{ij}$  - depend on crack orientation ( $\alpha, \theta^*$ ), shape, material properties (and V-notch opening angle  $\omega$ ).  $H_{ij}$ 's throughout this work address circular virtual cracks only, and  $\omega = 315^\circ$ . They are independent of virtual crack size, location  $z$  and general specimen geometry. As  $\nu$  is further away from 0.3, the simplification of  $H_{ij} \approx H_{ji}$  for  $j \neq i$  may no longer hold.

Clearly, the separation of variables enabled by the asymptotic expansion for  $\delta\Pi$  has significantly decreased the amount of required calculations.

$E, \nu, \sigma_c, \mathcal{G}_c$  - material properties, *criterion requires the knowledge of 4 material parameters.*

$S$  - depends on all the parameters which  $\sigma_{n,avg}$  depends on, namely crack orientation ( $\alpha, \theta^*$ ), location  $z$ , force  $F$ , general geometry (through  $A_i(z)$ ) and material properties ( $E, \nu, \sigma_c$ ). Consequently, the virtual crack area  $S$  also depends on all the parameters listed above, and therefore should not be mistaken for a material parameter.

The predicted failure plane **orientation** at a given  $z$  would change if the following data change:

$A_i(z)$  - for different geometries/far loading conditions.

$\nu$  - for different materials ( $\sigma_{n,int}$  is independent of  $E$ ).

The predicted failure **load** at a given  $z$  would change if the following data change:

$A_i(z)$  - for different geometries/far loading conditions.

$\nu, \sigma_c, \mathcal{G}_c$  - for different materials.

$H_{ij}$  - for different ( $E, \nu$ ).

## **6. Experiments on PMMA, Graphite and MACOR specimens with slanted V-notches**

Four-point-bending (4PB) experiments were conducted on bar-shaped specimens with a V-notch inclined to the specimen free surface (see Fig. 6). This geometry creates a mixed mode state of stress in the vicinity of the edge front [39, 40, 20, 29].

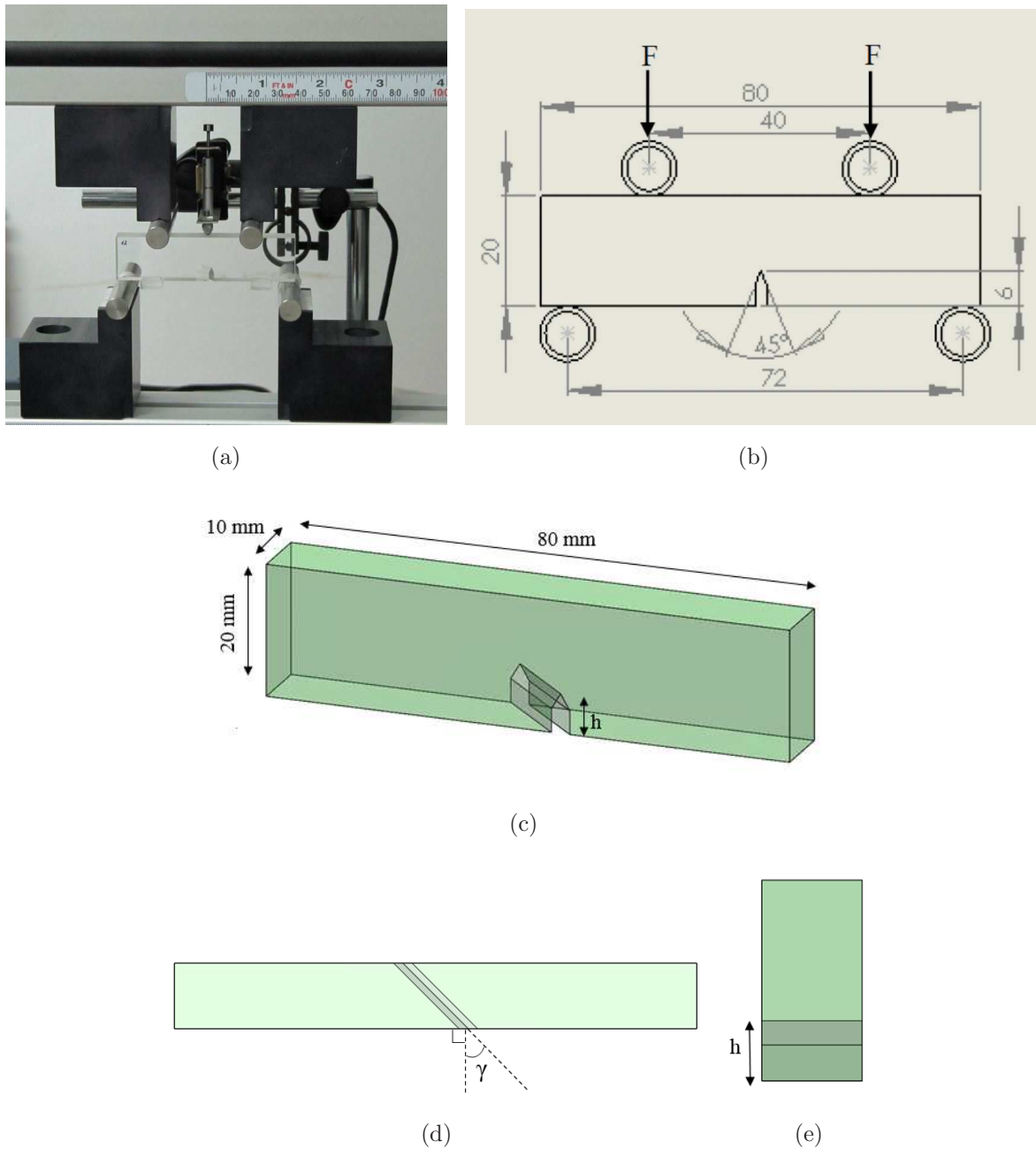


Figure 6: (a,b) 4PB experiment configuration. (c) Specimen's dimensions. (d) Top view (inclination angle  $\gamma = 30^\circ$ ). (e) Side view.

The specimen's dimensions are  $80 \times 20 \times 10 \text{ mm}$  with a V-notch with an opening angle of 45 degrees ( $\omega = 315^\circ$ ). Three inclination angles were considered  $\gamma = 0^\circ, 30^\circ, 45^\circ$ , with notch height of  $h = 6 \text{ mm}$  (in PMMA specimens  $h = 4 \text{ mm}$  was examined also).

For a small tip radius, we may assume a sharp notch [8], so the V-notches were machined with a cutting disc (2 mm thickness) having a tip radius of  $\rho = 50\mu\text{m}$  and a 45 degrees opening angle. In practice, the radius of curvature at the tip of the specimen's notches was within the range of 50 – 120  $\mu\text{m}$  in PMMA specimens (the difference in the radius resulted from the cutting entrance direction).

The specimens were manufactured from three materials considered linear elastic, homogeneous and isotropic.

1. Cast commercial PMMA (considered brittle at ambient temperatures).
2. Graphite manufactured by HIP (hot isostatic pressing) with small grain size (maximum 50  $\mu\text{m}$ ) by David Hart Ltd, UK (H2878 Graphite plate).
3. MACOR, a ceramic suitable for machining by Corning Inc. NY, USA, (Aremcolox 502-MACOR).

Experiments on the PMMA were performed using a Zwick 1445 machine (Zwick GmbH & Co. KG., Germany, 1992), with nominal load capability of 10kN. Experiments on the Graphite and MACOR were performed using a Shimadzu machine with nominal load capability of 20kN. All experiments were performed under a constant displacement rate of 1 mm/min (quasi-static). A Vishay system 7000 was used to record the load cell output (precision of  $\pm 0.5\%$  N) and displacements at the center of the specimen upper facet, by means of linear displacement sensors (LDS, with a precision of  $\pm 0.05\text{ mm}$ ). To assure the accuracy, attention has been paid to the parallel and center placements of the specimens in all directions.

### 6.1. Material properties

The material properties of the commercial PMMA, MACOR and Graphite are summarized in Table 3. The critical stress for fracture  $\sigma_c$  was estimated by loading a non-notched beam in 4PB until failure. The critical energy release rate  $\mathcal{G}_C$  was estimated based on mode I experiments on V-notched specimens using Leguillon's criterion for sharp V-notches and its correction for blunt V-notches [10].

Young's modulus  $E$  was measured by several methods for each material:

1. 4PB tests were performed on the V-notched beams with different inclination angles, as previously described. For each geometry a corresponding FE model was constructed. For each specimen the slope of the force-displacement curve was estimated, averaged for each geometry and compared to FE results. The value of  $E$  which gave the smallest error compared to the experiments was chosen.
2. In addition, 4PB tests were performed on non-notched beam specimens and compared with corresponding FE models. The specimens were repeatedly loaded to small loads up to 500 N. As for the notched beams, deflection was measured at the middle of the upper facet and the slope of the force-displacement curve was estimated in the linear region, averaged and compared to the FE results. The value of  $E$  which gave the smallest error compared to the experiments was chosen. These tests were usually repeated for several specimens, on alternating facets, to ensure the specimens are homogeneous and isotropic.
3. Ultrasonic testing - longitudinal and transverse velocities of ultrasonic waves were measured. The relation between the longitudinal wave velocity  $V_L$ , transverse wave velocity  $V_T$ , Young's modulus  $E$ , Poisson's ratio  $\nu$  and the density  $\rho$  is [41]:

$$V_L = \sqrt{\frac{E(1-\nu)}{\rho(1+\nu)(1-2\nu)}}, \quad V_T = \sqrt{\frac{E}{2\rho(1+\nu)}} \quad (10)$$

In the Graphite and MACOR experiments, the displacements measured at the center of the specimens upper facet by the LDS, were within experimental error range. Thus the estimation of  $E$  from mechanical testing is disqualified. Ultrasonic determination of  $E$  was instead used for all three materials (marked in bold in Table 3).

Material	$\sigma_c$ MPa	$E$ GPa		$\nu$	$G_C$ MPa mm	
		ultrasonic	mechanical		ultrasonic	mechanical
PMMA	103.3	<b>5.6</b>	3.9	0.332	<b>0.411</b>	0.601
Graphite	48	<b>10.8</b>	-	0.2	<b>0.118</b>	-
MACOR	159	<b>66.9</b>	-	0.25	<b>0.0329</b>	-

Table 3: Summary of material properties. Values used for the prediction of the failure law are boldface.



Experimental determination of  $\mathcal{G}_c$  was not possible (insertion of an initial crack to determine  $K_{IC}$  is very difficult in ceramic materials so these were not performed by us nor provided by the manufacturer). Therefore we computed  $\mathcal{G}_c$  using V-notched specimens under mode I loading by the methods in [7, 42] (see for details Appendix A. Since both  $\mathcal{G}_c$  and  $H_{ij}$  depend linearly on  $E$ , it has no influence on the computed  $\mathcal{G}_c$ ).

### 6.2. Measuring the failure initiation angles

There is no established generally accepted method to measure the angles of the planes at which failure initiates on the fractured surfaces. We chose to measure these angles based on a blue-light scan.

Several representative broken surfaces were scanned with an “ATOS Compact Scan 5M” optical blue light scanner (manufactured by GOM, Germany). A point-cloud that represent the surface of the right broken parts was converted to a smooth-surface file which was exported to a SolidWorks<sup>2</sup> program. The location of each crack origin and a small area according to which its orientation was determined were chosen by the authors. A tangential plane was defined through a chosen point in each small representative area, a normal axis was attached to each plane, and the angles  $(\alpha, \theta^*)$  were calculated externally (using Mathematica program) with respect to the V-notch bi-sector normal.

Measurements of the crack origin locations and orientations for all experiments are presented in Appendix B. The MACOR scanned surfaces seem to be the least reliable since significant changes in the fracture surface orientation were observed close to the V-notch edges. These specimens also had visible damage from the V-notch machining in the vertices region. Forces at fracture are also detailed in Appendix B.

### 6.3. Summary of experimental results

The experimental results for commercial PMMA, MACOR and Graphite are summarized in Tables 4 and 5.

---

<sup>2</sup>SolidWorks is a trademark of Dassault Systèmes SolidWorks Corporation in the US and other countries.

$\gamma^\circ$	Avg. number of fracture origins		
	PMMA	Graphite	MACOR
0	multiple (along entire edge)	multiple (along entire edge)	multiple (along entire edge, 9 main)
30	several (4-8 main, mainly edge center)	multiple (about 18, 6 main)	multiple (about 15, 8 main)
45	single (irregular location)	multiple (about 12, 4 main)	multiple (about 10, 5 main, distributed over 2/3 edge)

Table 4: Average number of fracture origins in different V-notch inclinations in PMMA, Graphite and MACOR specimens with  $h = 6 \text{ mm}$ .

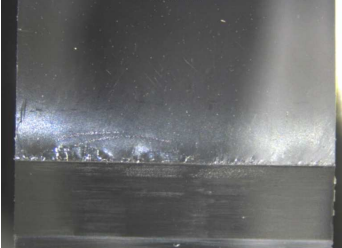

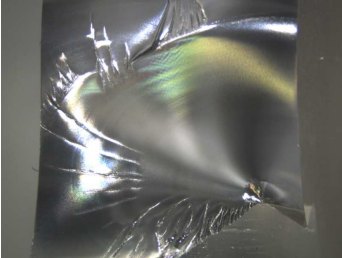
# of specimens, $\gamma^\circ$	Avg. force @ fracture N (deviation)	Representative fracture surface
5, $0^\circ$	922 ( $\pm 64$ )	
4, $30^\circ$	1213 ( $\pm 63$ )	
4, $45^\circ$	1604 ( $\pm 103$ )	

Table 5: PMMA: Average force at fracture,  $h = 6 \text{ mm}$  (stereoscope,  $\times 8$ ).

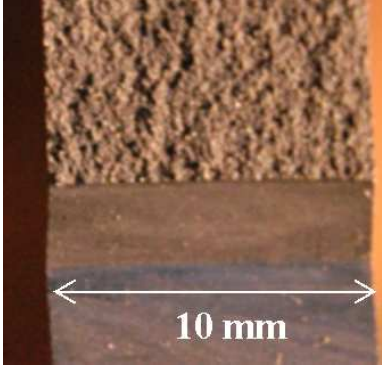
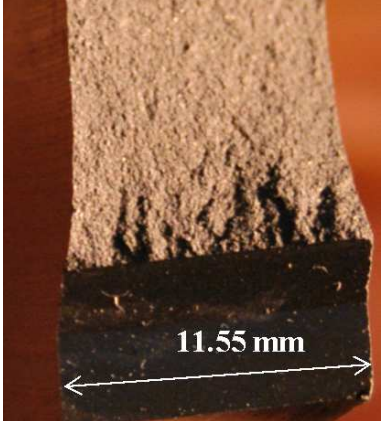
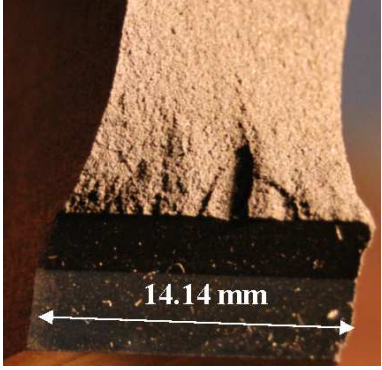
# of specimens, $\gamma^\circ$	Avg. force @ fracture N (deviation)	Representative fracture surface
1, $0^\circ$	668	
5, $30^\circ$	846 ( $\pm 19$ )	
5, $45^\circ$	1028 ( $\pm 24$ )	

Table 6: Graphite: Average force at fracture,  $h = 6 \text{ mm}$ .


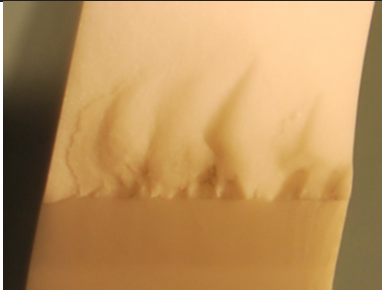
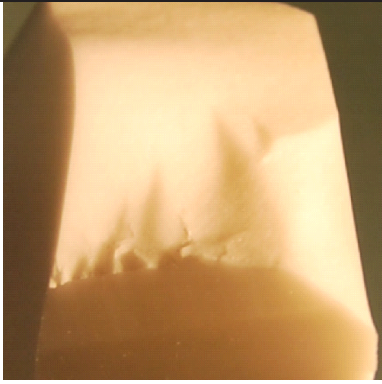
# of specimens, $\gamma^\circ$	Avg. force @ fracture N (deviation)	Representative fracture surface
1 , $0^\circ$	996 ( $\pm 112$ )	
5 , $30^\circ$	1290 ( $\pm 189$ )	
5 s, $45^\circ$	1489 ( $\pm 44$ )	

Table 7: MACOR: Average force at fracture,  $h = 6 \text{ mm}$ .

For all 3 materials and geometries, the experimental force at fracture is within a small deviation from the average - under 7% in the PMMA, under 3% in the Graphite and under 14% in the MACOR specimens.

One may observe in PMMA specimens a connection between the inclination angle  $\gamma$  and the number of fracture origins - as  $\gamma$  increases the number of origins decreases. This trend was not observed at all in the Graphite specimens, while in the MACOR specimens a decrease in the number of origins was observed for  $\gamma = 45^\circ$ .

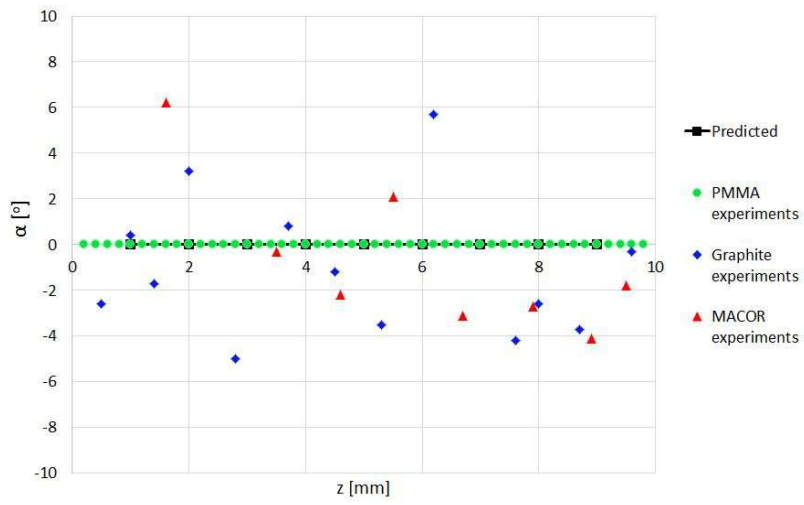
## 7. Comparison between predicted failure initiation force and angles and experimental observations

The prediction of failure load and failure initiation angles, of the newly formulated 3-D criterion are compared to the experimental observations to examine the validity of the criterion.

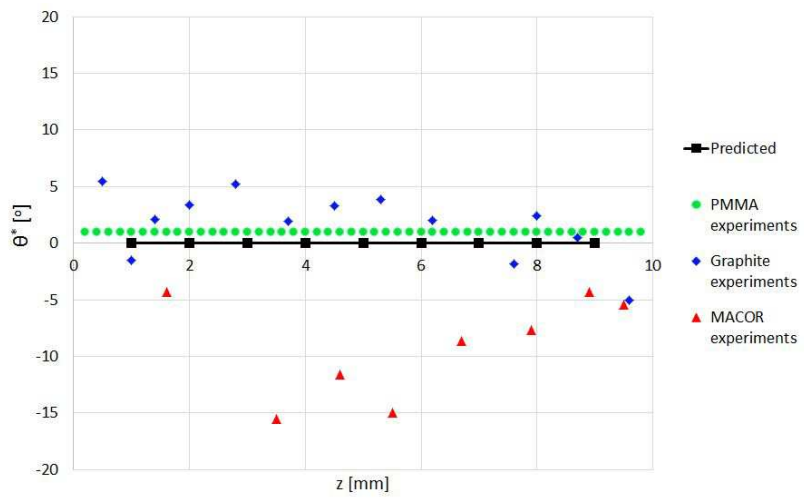
### 7.1. Failure initiation angles

The failure initiation orientation was determined by the maximum average normal stress  $\sigma_{n,avg}$  (7) at intervals of 1 mm along the V-notch edge ( $z$ ) over a circular sector of a constant size ( $0.1 \text{ mm}^2$ ) and a reference force of 1000 N.

Predicted and experimental results are presented in Figures 7-9 for PMMA, Graphite and MACOR. For  $\gamma = 0^\circ$  and  $30^\circ$ , the predicted angles were identical for all 3 materials and therefore represented by a single solid curve with square markers. At  $\gamma = 45^\circ$  there was some variation between the predicted  $\alpha, \theta^*$  so each material was represented by a separate curve (PMMA green circles, Graphite blue Rhombi and MACOR red triangles).  $\alpha$  and  $\theta^*$  correspond to the locations  $z$  at which they were measured.

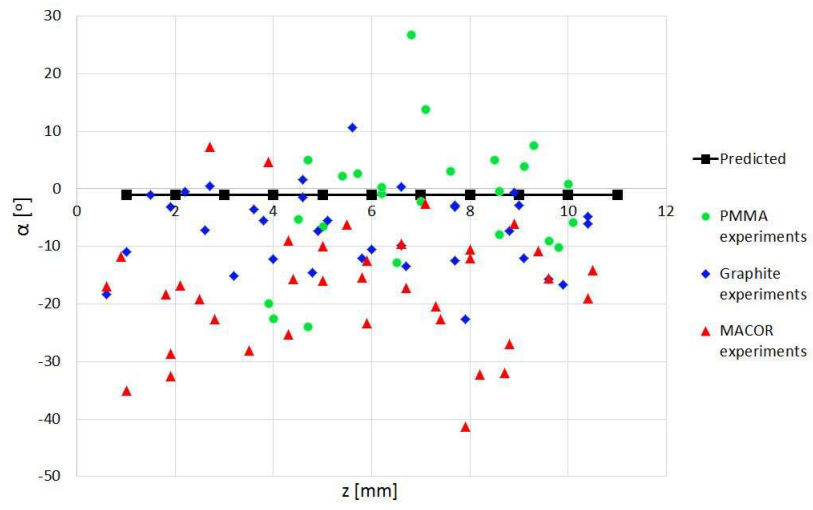


(a)

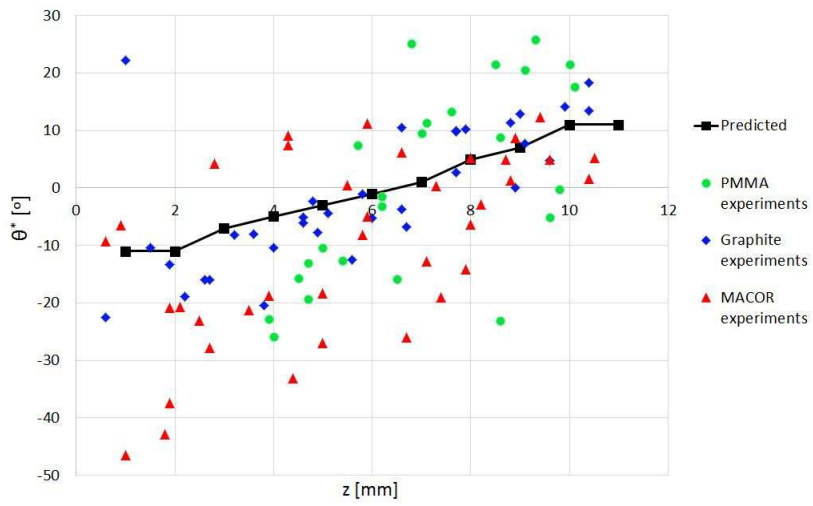


(b)

Figure 7: Predicted and experimental  $\alpha$  (a) and  $\theta^*$  (b) angles for  $\gamma = 0^\circ$ .

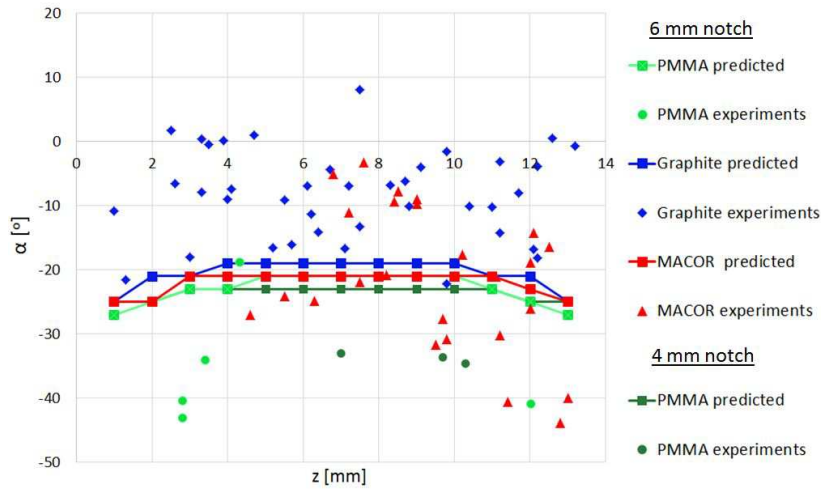


(a)

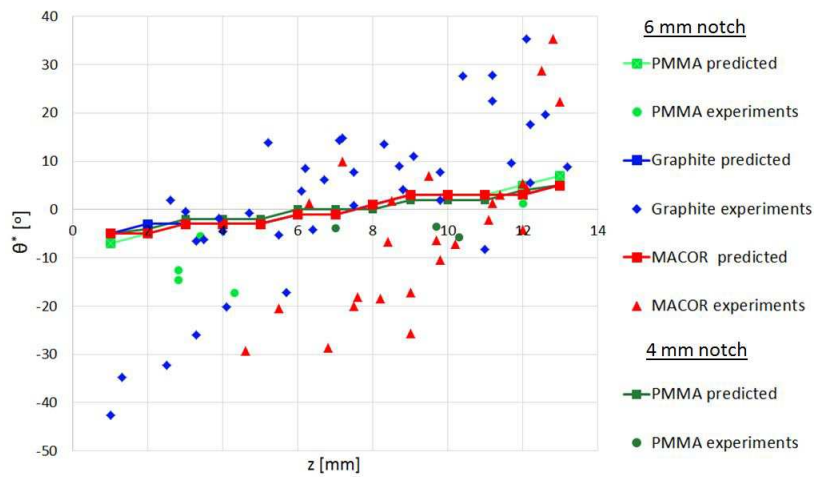


(b)

Figure 8: Predicted and experimental  $\alpha$  (a) and  $\theta^*$ (b) angles for  $\gamma = 30^\circ$ .



(a)



(b)

Figure 9: Predicted and experimental  $\alpha$  (a) and  $\theta^*$  (b) angles for  $\gamma = 45^\circ$ .

For the chosen  $\gamma$ s the predicted failure initiation angle  $\alpha$  is always negative or zero, and the non-zero values are significantly smaller compared to  $\theta^*$ .  $\alpha$  is symmetric with respect to the mid edge whereas  $\theta^*$  is anti-symmetric.

Changing  $E$  yield same predicted failure initiation angles  $(\alpha, \theta^*)$ . The orientation of maximum average normal stress changes very moderately with  $\nu$ , as observed in Fig. 7-9 ( $(\alpha, \theta^*)$  remained identical for the three materials for  $\gamma = 0^\circ$  and  $30^\circ$  and similar for  $\gamma = 45^\circ$ ).

A good agreement between the predicted and experimental results is observed for  $\gamma = 0^\circ$ . For  $\gamma = 30^\circ$ , one can observe that experimental values of  $\theta^*$  are negative at small  $z$  with a



gradual increase to positive values at larger  $z$ . This antisymmetrical trend with respect to the edge center is also predicted, but yet underestimates the experimental observations.  $\alpha$  is mostly negative, whereas the predicted ones are approximately zero. This indicates that  $A_1(z)$  is more dominant for this geometry compared with  $A_3(z)$ , contrary to the experimental observations. An error in the numerically obtained functions  $A_i(z)$  could decrease the relation  $\frac{A_3(z)}{A_1(z)}$ , which draws  $\alpha$  to zero as in pure mode I.

For  $\gamma = 45^\circ$ , the antisymmetrical trend of  $\theta^*$  with respect to the mid edge is again observed, however the predicted values still significantly underestimate the experimental ones. The predicted  $\alpha$ s are negative, as are most of the experimental measurements and are smaller in the outer portions of the V-notch edge - this trend is observed in experiments also. For all three materials, the predicted  $\alpha$ s are within the experimental range. They mostly overestimate PMMA experimental observations, mostly underestimate Graphite experimental observations, and are approximately in the middle of the MACOR experimental range.

One combination of  $(\alpha, \theta^*)$  at a given  $z$  corresponds to the maximum average normal stress  $\sigma_{n,avg}$ . For example,  $\sigma_{n,avg}$  for PMMA for a large range of  $(\alpha, \theta^*)$  is shown in Fig. 10 for  $\gamma = 45^\circ$ ,  $z = 5\text{ mm}$ . In the vicinity of the maximum  $\sigma_{n,avg}$  changes very moderately. Therefore there is a large range of  $(\alpha, \theta^*)$  combinations that result in 5% of the maximum value of  $\sigma_{n,avg}$  as shown in Fig. 11. The approximate range is  $-39^\circ \leq \alpha \leq 0^\circ$ ,  $-15^\circ \leq \theta^* \leq 12^\circ$ , which means that the presence of any small local defect may have a significant influence on the failure initiation orientation. This may explain some of the differences between the predicted and experimental failure initiation angles.

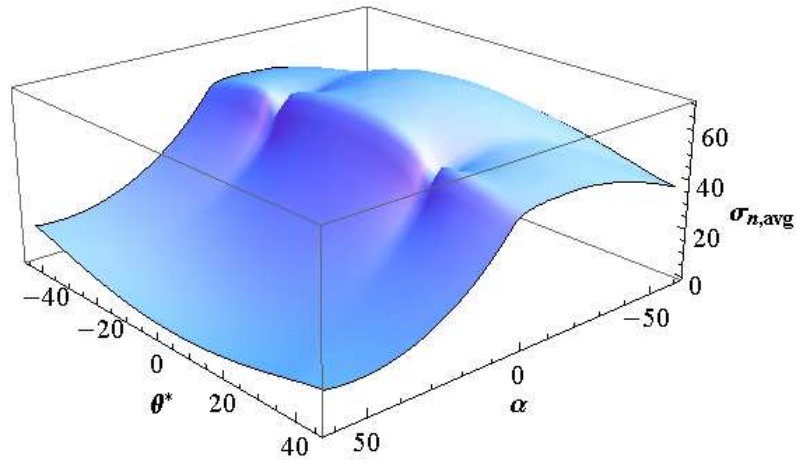


Figure 10:  $\sigma_{n,avg}$  for PMMA as a function of  $(\alpha, \theta^*)$  for  $\gamma = 45^\circ$ , at  $z = 5 \text{ mm}$

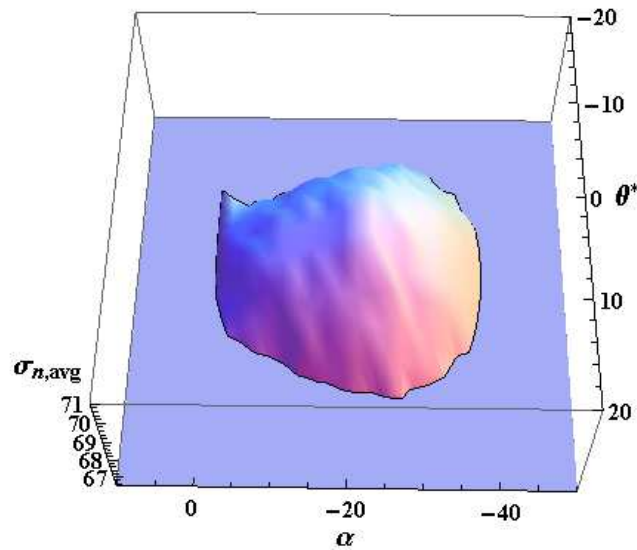


Figure 11:  $(\alpha, \theta^*)$  for which  $\sigma_{n,avg}$  is within 5% of its maximum value. PMMA,  $\gamma = 45^\circ$ , at  $z = 5 \text{ mm}$ .

## 7.2. Failure load

The minimum force that satisfies simultaneously (8) and (9) along the V-notch edge is the predicted failure load. In Fig. 12-14, the predicted loads within 5% of the minimum value are presented along with experimental results for PMMA, Graphite and MACOR. Specimens that were not scanned to determine failure initiation locations and angles, but their force at

fracture was measured, are represented by dashed lines. Since the location of the fracture origin could not be determined for these specimens, the dashed lines in Fig. 12-14 extend vertically throughout most of the V-notch front. We emphasize that this representation does not indicate anything about the location of failure initiation, and only provides information about the force at the moment of failure.

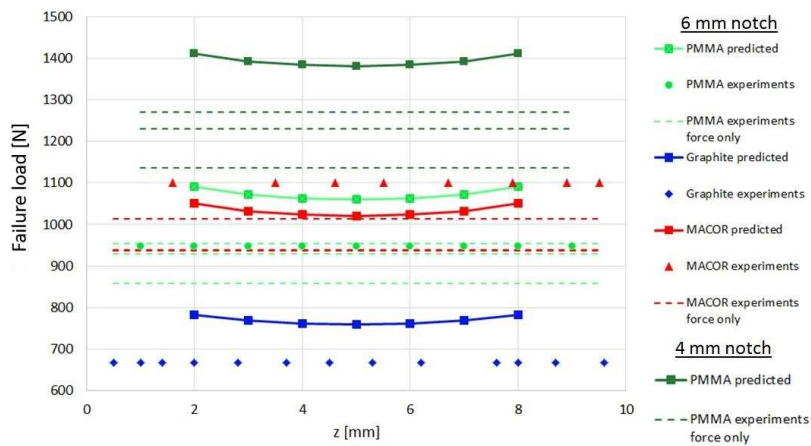


Figure 12: Predicted and experimental failure load in  $\gamma = 0^\circ$  specimens.

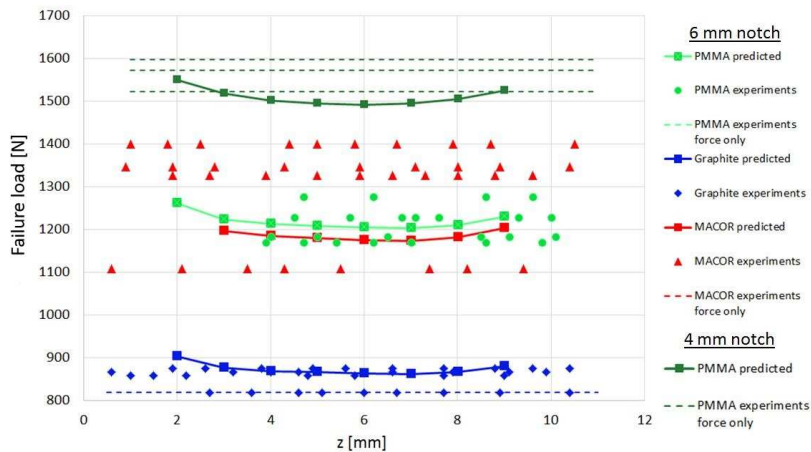


Figure 13: Predicted and experimental failure load in  $\gamma = 30^\circ$  specimens.

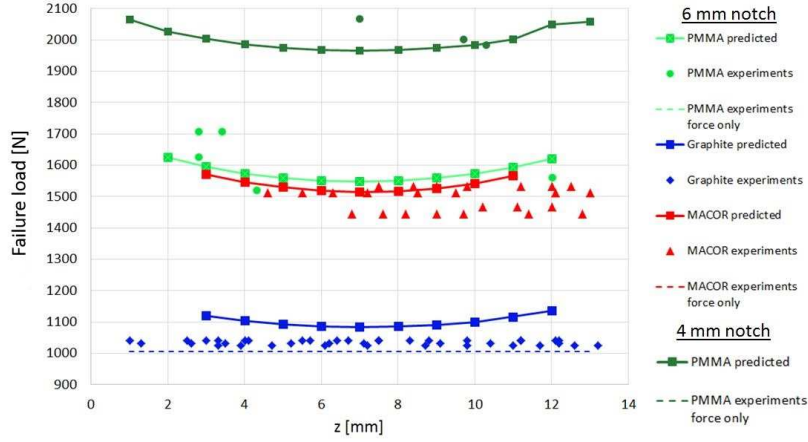


Figure 14: Predicted and experimental failure load in  $\gamma = 45^\circ$  specimens.

Predicted failure loads are very close to the experimental ones. In specimens with  $\gamma = 0^\circ$  made of PMMA and Graphite the failure load overestimates the experimental one, and in  $\gamma = 45^\circ$  for Graphite specimens the predicted load also slightly overdetermines the experimental ones. For all other geometries and materials, the predicted failure loads are close to the experimental ones. The RMS (root-mean-square) error for each geometry and material is summarized in Table 8.

There are different relations between the three loading modes (expressed through  $A_1(z)$ ,  $A_2(z)$ ,  $A_3(z)$ ). As  $\frac{A_3(z)}{A_1(z)}$  and  $\frac{A_2(z)}{A_1(z)}$  increase, the failure load increases. Therefore, failure load increases with  $\gamma$ . The failure load does not change significantly along most of the V-notch edge. The relation  $\frac{A_3(z)}{A_1(z)}$  for  $\gamma = 45^\circ$  is larger compared to  $\gamma = 30^\circ$ . In the experiments the edge portion at which failure initiates was reduced as  $\gamma$  increased for PMMA and for MACOR, but not for Graphite.

Table 8 shows that the predicted failure loads match well the experimental observations. For  $\gamma = 30^\circ$  and  $45^\circ$ , the RMS difference is mostly under 6.5%. The difference is larger for the  $\gamma = 0^\circ$  geometry. The approximation of the virtual crack by a circular area may not be appropriate for this case.

For comparison, predicted and experimental failure loads for in plane mode I and mixed in plane modes I and II (results from [2, 8]) are provided in Table 9 for the case of  $\omega = 315^\circ$ .

Material	$h$ mm	$\gamma$	$\frac{A_2}{A_1}, \frac{A_3}{A_1}$ at min. force	Min. force at fracture from (9) N	difference range compared with experiments	RMS error compared with experiments
PMMA	6	$0^\circ$	0,0	1060	-23.4% to -11.1%	15.9%
	6	$30^\circ$	-0.016,-0.45	1206	-3.2% to 5.5%	3.5%
	6	$45^\circ$	0.003,-0.87	1548	-1.8% to 9.3%	5.3%
	4	$0^\circ$	0,0	1381	-21.4% to -8.6%	15.1%
	4	$30^\circ$	-0.005,-0.59	1493	1.9% to 6.6%	4.9%
	4	$45^\circ$	0.002,-0.92	1966	0.9% to 4.9%	3%
Graphite	6	$0^\circ$	0,0	760	-13.8%	13.8%
	6	$30^\circ$	-0.016,-0.45	862	-5.5% to 0.3%	3.9%
	6	$45^\circ$	0.003,-0.87	1084	-7.8% to -4.2%	6.3%
MACOR	6	$0^\circ$	0,0	1020	-9% to -0.7%	7.2%
	6	$30^\circ$	-0.016,-0.45	1174	-6% to 16.1%	12.1%
	6	$45^\circ$	0.003,-0.87	1515	-4.8% to 1.1%	3%

Table 8: Difference between predicted and experimental failure load for  $h = 6\text{ mm}$  and  $\gamma = 0^\circ, 30^\circ, 45^\circ$  for all materials examined.

Comparing the % difference of force in in-plane loading from Table 9 with the % difference in 3-D loading under modes I+II+III in Table 8, one notices that the new generalized 3-D criterion predicts the failure load with a higher accuracy. In the presence of mode III ( $\gamma \neq 0^\circ$ ) the precision of the predicted failure load is consistently improved compared to the experimental results (with one geometry excluded,  $\gamma = 30^\circ$  in MACOR).

In Table 8 pure mode I ( $\gamma = 0^\circ$  geometry) was also determined by the 3-D criterion. It should be noted, that the 3-D criterion, which is applicable for all combinations of modes I+II+III, *does not reduce to the 2D form* of the Yosibash et. al and Leguillon's criteria [7, 8]. This is most notably due to the representation of the virtual crack and its vicinity: in the 2-D criteria the virtual crack is represented by a line and its vicinity is a circular area, whereas in the generalized 3-D criterion presented herein, the virtual crack is represented by a circular sector and its vicinity is a sphere (for details see [33]).

The sensitivity of the results of the 3-D criterion to  $E, \sigma_c$  and  $\mathcal{G}_c$  was examined assuming all other material parameters are constant. This check was performed for 6mm45deg geom-

Material	$\frac{A_2}{A_1}$	$\theta^*$ % difference between predictions and experiments	failure load % difference between predictions and experiments
PMMA <i>(slanted: exp. at -75°C)</i>	0	-	37.8%
	0.07	1.2%	-19.3%
	0.156	3.8%	-23.6%
	0.217	6.9%	-19.6%
	0.333	7.4%	-18.6%
	0.616	5%	-17.5%
	<i>0.11</i>	<i>-2.3%</i>	<i>-5.3%</i>
	<i>0.19</i>	<i>3.9%</i>	<i>0.4%</i>
	<i>0.29</i>	<i>0%</i>	<i>4.7%</i>
	<i>0.53</i>	<i>5%</i>	<i>15.5%</i>
	<i>0.686</i>	<i>11.1%</i>	<i>16.1%</i>
MACOR	0.342	4.3%	-0.3%
	1.308	8.7%	15.3%
	1.737	-6.2%	20.9%
	2.2	-13%	6.5%
	3.25	3%	6.1%

Table 9: Experimental and predicted data for a mode I and mode II in-plane criteria [2, 8] for  $\omega = 315^\circ$ . Experiments performed at  $-75^\circ C$  are in slanted.

etry and PMMA material properties. None of these parameters influence the orientation angles ( $\alpha, \theta^*$ ). Increasing  $E$  or  $\mathcal{G}_c$  by 10% increased the the minimum force at fracture by 4.6%.  $\sigma_c$  had a significantly smaller influence, increasing the minimum force at fracture only by 0.7% when  $\sigma_c$  was increased by 10%. Therefore, the overestimation of the force at fracture by the criterion may be attributed to the overestimated value of  $E$  from the ultrasonic testing (which in our experience is by about 20-30% compared with mechanically obtained values). The influence of  $E$  is apparently more significant than the approximation of the blunt V-notch tip to a sharp one, which is expected to under-determine the experimental results.

Importantly, the virtual crack area  $S$  obtained in the calculations of the 3-D criterion

(7,9) is small compared to the specimen dimensions (at least 20 times smaller than the V-notch edge length), as required by the asymptotic expansion. Values of  $S$  for all materials and geometries examined are presented in Table 10.

Material	$h$ mm	Inclination angle	$S$ of the virtual crack $mm^2$
PMMA	6	$\gamma = 0^\circ$	$0.149 \leq S \leq 0.15$
	6	$\gamma = 30^\circ$	$0.108 \leq S \leq 0.119$
	6	$\gamma = 45^\circ$	$0.112 \leq S \leq 0.125$
	4	$\gamma = 0^\circ$	$S = 0.149$
	4	$\gamma = 30^\circ$	$0.084 \leq S \leq 0.095$
	4	$\gamma = 45^\circ$	$0.113 \leq S \leq 0.122$
Graphite	6	$\gamma = 0^\circ$	$0.84 \leq S \leq 0.862$
	6	$\gamma = 30^\circ$	$0.652 \leq S \leq 0.691$
	6	$\gamma = 45^\circ$	$0.599 \leq S \leq 0.652$
MACOR	6	$\gamma = 0^\circ$	$0.022 \leq S \leq 0.022$
	6	$\gamma = 30^\circ$	$0.018 \leq S \leq 0.019$
	6	$\gamma = 45^\circ$	$0.016 \leq S \leq 0.017$

Table 10: The range of the virtual crack area  $S$  obtained by the 3-D criterion , for  $h = 6\text{ mm}$  and  $\gamma = 0^\circ, 30^\circ, 45^\circ$  for all materials examined.

### 7.3. A failure criterion based entirely on the ERR and stress requirements

Although the ERR criterion alone cannot predict correctly the failure initiation orientation in 3-D we examined if the requirement of simultaneously satisfying both stress and ERR conditions may well predict both orientation and load to failure. The crack shape was still assumed to be a circular sector. The computations were realized by means of a code written in ‘‘Mathematica’’. The force  $F$  and orientation  $(\alpha, \theta^*)$  were taken in intervals. For a given force, and combinations of  $(\alpha, \theta^*)$  taken in intervals between  $-61^\circ \leq \alpha \leq 61^\circ$ ,  $-45^\circ \leq \theta^* \leq 45^\circ$ , we found numerically the radius of a circular sector which fulfills:

$$\sigma_c \times 0.95 < \frac{\int \sigma_n(r_p, \theta_p) r_p dr_p d\theta_p}{\int r_p dr_p d\theta_p} < \sigma_c \times 1.05 \quad (11)$$

A 10% range was allowed for numerical errors. If such radius existed for the specific force and orientation, the estimated virtual crack area  $S$  was substituted into the expression of  $\mathcal{G}$ . It was examined whether this value lies within  $\pm 10\%$  of  $\mathcal{G}_c$ :

$$\begin{aligned} \mathcal{G}_c \times 0.9 < F \left( \tilde{A}_1^2(z) \times (\sqrt{S})^{2\alpha_1-1} H_{11}(\alpha, \theta^*) + \tilde{A}_1(z) \tilde{A}_2(z) \times (\sqrt{S})^{\alpha_1+\alpha_2-1} \times (H_{12}(\alpha, \theta^*) + H_{21}(\alpha, \theta^*)) \right. \\ + \tilde{A}_2^2(z) \times (\sqrt{S})^{2\alpha_2-1} H_{22}(\alpha, \theta^*) + \tilde{A}_1(z) \tilde{A}_3(z) \times (\sqrt{S})^{\alpha_1+\alpha_3-1} \times (H_{13}(\alpha, \theta^*) + H_{31}(\alpha, \theta^*)) \\ \left. + \tilde{A}_2(z) \tilde{A}_3(z) \times (\sqrt{S})^{\alpha_2+\alpha_3-1} \times (H_{23}(\alpha, \theta^*) + H_{32}(\alpha, \theta^*)) + \tilde{A}_3^2(z) \times (\sqrt{S})^{2\alpha_3-1} H_{33}(\alpha, \theta^*) \right) < \mathcal{G}_c \times 1.1 \end{aligned} \quad (12)$$

The combinations of orientation angles and force which fulfills both (11) and (12) were documented. At forces smaller than a certain value, no radius of the circular sector has fulfilled both (11,12). The process was repeated until this minimum value of the force was reached. This force was taken as the force for failure.

This criterion was examined for 2 cases:  $z = 5 \text{ mm}$  for pure mode III loading, and  $z = 7 \text{ mm}$  at  $\gamma = 45^\circ$ , both for PMMA. For pure mode III, the orientations which fulfilled (11,12) were within  $-26^\circ \leq \alpha \leq -6^\circ, -11^\circ \leq \theta^* \leq 9^\circ$ , whereas we expected  $(\alpha, \theta^*) \sim (-45^\circ, 0^\circ)$ . For the  $\gamma = 45^\circ$  configuration the minimum failure load was  $1360 \text{ N}$  and  $-6^\circ \leq \alpha \leq 1^\circ, -11^\circ \leq \theta^* \leq 9^\circ$  whereas the average failure load in experiments was  $1604 \text{ N}$  (compare to  $1548 \text{ N}$  in Table 8). We therefore concluded that this alternative criterion is inferior to the one already presented.

## 8. Summary and conclusions

A new 3-D failure initiation criterion from sharp V-notches suitable for general loading conditions (modes I+II+III) was presented. It predicts both failure initiation angles  $(\alpha, \theta^*)$  and load to failure  $F$ . The crack initiation orientation is determined exclusively by the maximum average normal stress along the V-notch edge ( $z$ ). The criterion was validated by experimental observations on three quasi-brittle materials, PMMA, Graphite and MACOR. Several mode mixities were examined (expressed through  $A_1(z), A_2(z), A_3(z)$ ). The predicted failure initiation angles are similar to experimental trends and predict the observations well for  $\gamma = 0^\circ$  and  $\gamma = 45^\circ$ . The predicted loads at failure were under 16% deviation (in terms of RMS) from the experimental results for all three materials and all geometries, and



mostly under 6.5% for  $\gamma = 30^\circ$  and  $45^\circ$ . A better determination of  $E$  is expected to further reduce this deviation. The newly introduced criterion is therefore suited for predicting failure initiation in 3-D brittle elastic V-notched structures.

The criterion involves several simplifying assumptions:

1. Failure initiates along the V-notch edge (vertices excluded).
2. Only initiation (and not propagation) of failure is predicted.
3. It is applicable to quasi-brittle materials, such as glasses, ceramics, and certain kinds of polymers (for which plastic deformation can be neglected). The material is also assumed to be homogeneous and isotropic.
4. Quasi-static load (no dynamic considerations included).
5. V-notch surfaces are traction-free.
6. A sharp V-notch is assumed. One can extend the proposed criterion to investigation of the influence of the V-notch tip radius on the predicted failure loads and reformulate the proposed criterion to account for it, as in [42, 43].
7. The virtual crack is assumed to be planar.
8. The virtual crack shape is assumed to be a circular sector, although the curves  $\sigma_n = \sigma_c$  defining the crack shape are of a complex “peanut-shape” form. “Peanut-shaped” virtual cracks may increase the accuracy of the predictions (but will significantly increase the complexity of the calculations).

Future experimental observations on specimens with V-notch opening angles of  $300^\circ$ ,  $330^\circ$  and  $270^\circ$  will enable to determine the broader application of the proposed criterion. At the same time, future investigation on the implementation of  $\mathcal{G}_c$  in modes II and III (usually denoted  $\mathcal{G}_{IIc}$  and  $\mathcal{G}_{IIIc}$ ) into the failure criterion may improve its predictability.

**Acknowledgements:** The authors would like to thank prof. Dominique Leguillon from Univ. Pierre and Marie Curie, Paris, for stimulating discussions on the topic and Mr. Ilan Gilad for his assistance in performing the experiments. This research was supported by the Israel Science Foundation (grants No. 444/10 and 593/14).

## References

- [1] P. Lazzarin and R. Zambardi. A finite-volume-energy based approach to predict the static and fatigue behavior of components with sharp V-shaped notches. *International Journal of Fracture*, 112:275–298, 2001.
- [2] Z. Yosibash, A. Bussiba, and I. Gilad. Failure criteria for brittle elastic materials. *International Journal of Fracture*, 125:307–333, 2004.
- [3] F. Berto, P. Lazzarin, and M.R. Ayatollahi. Brittle fracture of sharp and blunt V-notches in isostatic graphite under torsion loading. *Carbon*, pages 1942–1952, 2012.
- [4] F. Berto and P. Lazzarin. Recent developments in brittle and quasi-brittle failure assessment of engineering materials by means of local approaches. *Materials Science and Engineering: R: Reports*, 75:1 – 48, 2014.
- [5] A. Seweryn. Brittle fracture criterion for structures with sharp notches. *Engineering Fracture Mechanics*, 47:673–681, 1994.
- [6] M.R. Ayatollahi, A.R. Torabi, and P. Azizi. Experimental and theoretical assessment of brittle fracture in engineering components containing a sharp V-notch. *Experimental Mechanics*, 51:919–932, 2011.
- [7] D. Leguillon. Strength or toughness? a criterion for crack onset at a notch. *European Journal of Mechanics - A/Solids*, 21:61–72, 2002.
- [8] Z. Yosibash, E. Priel, and D. Leguillon. A failure criterion for brittle elastic materials under mixed-mode loading. *International Journal of Fracture*, 141:291–312, 2006.
- [9] E. Priel, A. Bussiba, I. Gilad, and Z. Yosibash. Mixed mode failure criteria for brittle elastic V-notched structures. *International Journal of Fracture*, 144:247–265, 2007.
- [10] Z. Yosibash. *Singularities in Elliptic Boundary Value Problems and Elasticity and their Connection with Failure Initiation*. Springer, 2012.

- [11] A. Sapora, P. Cornetti, and A. Carpinteri. A finite fracture mechanics approach to V-notched elements subjected to mixed-mode loading. *Engrg. Frac. Mech.*, 97:216 – 226, 2013.
- [12] A. Sapora, P. Cornetti, and A. Carpinteri. V-notched elements under mode II loading conditions. *Structural Engineering and Mechanics*, 49:499–508, 2014.
- [13] P. Cornetti, A. Sapora, and A. Carpinteri. Mode mixity and size effect in V-notched structures. *Int. Jour. Solids and Structures*, 50:1562–1582, 2013.
- [14] A. Seweryn and A. Lukaszewicz. Verification of brittle fracture criteria for elements with sharp v-shaped notches. *Engineering Fracture Mechanics*, 69:1487–1510, 2002.
- [15] M. L. Dunn, W. Suwito, S. Cunningham, and C. W. May. Fracture initiation at sharp notches under mode I, mode II, and mild mixed mode loading. *International Journal of Fracture*, 84:376–381, 1997.
- [16] V. Mantič and I.G. García. Crack onset and growth at the fibre–matrix interface under a remote biaxial transverse load. Application of a coupled stress and energy criterion. *Int. Jour. Solids and Structures*, 49:2273–2290, 2012.
- [17] J. Chang, J. Xu, and Y. Mutoh. A general mixed-mode brittle fracture criterion for cracked materials. *Engineering Fracture Mechanics*, 73:1249–1263, 2006.
- [18] Z. Yishu. Experimental study on mixed mode crack propagation. *Engineering Fracture Mechanics*, 34:891–899, 1989.
- [19] C.G. Sih and B. Macdonald. Fracture mechanics applied to engineering problems - strain energy density fracture criterion. *Engineering Fracture Mechanics*, 6:361–368, 1974.
- [20] V. Lazarus, F.G. Buchholz, M. Fulland, and J. Wiebesiek. Comparison of predictions by mode II or mode III criteria on crack front twisting in three or four point bending experiments. *International Journal of Fracture*, 153:141–151, 2008.

- [21] V. Lazarus, J.B. Leblond, and S.E. Mouchrif. Crack front rotation and segmentation in mixed mode I+III or I+II+III. Part I: calculation of stress intensity factors. *Journal of Mechanics and Physics of Solids*, 49:1399–1420, 2001.
- [22] V. Lazarus and J.B. Leblond. Crack paths under mixed mode (I+III) or (I+II+III) loadings. *Comptes Rendus de l’Academie des Sciences, Serie II*, 326:171–177, 1998.
- [23] L. Nobile. Mixed mode crack initiation and direction in beams with edge cracks. *Theoretical and Applied Fracture Mechanics*, 33:107–116, 2000.
- [24] F. Erdogan and G. Sih. On the crack extension in plates under loading and transverse shear. *Journal of Basic Engineering*, 85:519–527, 1963.
- [25] S. Suresh and C.F. Shih. Combined mode I - mode II and mode I - mode III fracture of brittle materials. *Scripta Metallurgica et Materialia*, 25:991–996, 1991.
- [26] S. Liu, Y. Chao, and X. Zhu. Tensile-shear transition in mixed mode I/III fracture. *International Journal of Solids and Structures*, 41:6147–6172, 2004.
- [27] D. Tian, D. Lu, and J. Zhu. Crack propagation under combined stresses in three dimensional medium. *Engineering Fracture Mechanics*, 16:5–17, 1982.
- [28] M. Schollmann, H.A. Richard, G. Kullmer, and M. Fulland. A new criterion for the prediction of crack development in multiaxially loaded structures. *International Journal of Fracture*, 117:129–141, 2002.
- [29] B. Lin, M. E. Mear, and K. Ravi-Chandar. Criterion for initiation of cracks under mixed-mode I+III loading. *International Journal of Fracture*, 165:175–188, 2010.
- [30] K.H. Pham and K. Ravi-Chandar. Further examination of the criterion for crack initiation under mixed-mode I+III loading. *International Journal of Fracture*, 189:121–139, 2014.
- [31] A. Kotousov, P. Lazzarin, F. Berto, and L.P. Pook. Three-dimensional stress states at crack tip induced by shear and anti-plane loading. *Engrg. Frac. Mech.*, 108:65 – 74, 2013.

- [32] S. Khan and M. Khraisheh. Analysis of mixed mode crack initiation angles under various loading conditions. *Engineering Fracture Mechanics*, 67:397–419, 2000.
- [33] B. Mittelman and Z. Yosibash. Asymptotic analysis of the potential energy difference because of a crack at a V-notch edge in a 3D domain. *Engrg. Frac. Mech.*, 131:232–256, 2014.
- [34] Z. Yosibash, N. Omer, M. Costabel, and M. Dauge. Edge stress intensity functions in polyhedral domains and their extraction by a quasilocal function method. *Int. Jour. Fracture*, 136:37 – 73, 2005.
- [35] B. Mittelman and Z. Yosibash. Energy release rate cannot predict crack initiation orientation in domains with a sharp V-notch under mode III loading. *Engrg. Frac. Mech.*, 141:230–241, 2015.
- [36] Brigit Mittelman. *A Failure Initiation Criterion from a Sharp V-notch Edge in 3D Elastic Brittle Structures*. PhD thesis, Ben-Gurion University of the Negev, 2015.
- [37] [www.bgu.ac.il/~zohary/MathematicaCodesFor3DFailureCriterion.pdf](http://www.bgu.ac.il/~zohary/MathematicaCodesFor3DFailureCriterion.pdf).
- [38] B.A. Szabo and I. Babushka. *Finite element analysis*. John Wiley and Sons, New York, 1997.
- [39] D. Leguillon. Computation of 3D singular elastic fields for the prediction of failure at corners. *Key Engineering Materials*, 251-252:147–152, 2003.
- [40] F.G. Buchholz, A. Chergui, and H.A. Richard. Fracture analyses and experimental results of crack growth under general mixed mode loading conditions. *Engineering Fracture Mechanics*, 71:455–468, 2004.
- [41] I.H. Sarpun, V. Ozkan, and S. Tuncel. Ultrasonic determination of elastic modulus of marbles relation with porosity and cao. *The 10 International Conference of the Slovenian Society for Non-Destructive Testing 'Application of Contemporary Non-Destructive Testing in Engineering' September 1-3 ,Ljubljana, Slovenia*, pages 119–125, 2009.

- [42] D. Leguillon and Z. Yosibash. Crack onset at a V-notch. Influence of the notch tip radius. *Int. Jour. Fracture*, 122:1–21, 2003.
- [43] E. Priel, Z. Yosibash, and D. Leguillon. Failure initiation at a blunt V-notch tip under mixed mode loading. *International Journal of Fracture*, 149:143–173, 2008.

## Appendix A. Determination of $\mathcal{G}_c$ by experiments on V-notched specimens under mode I

The critical stress  $\sigma_c$  is independent of  $E$ .  $A_{1C}$  does not depend on  $E$ , and  $H_{ij}^{new} = H_{ij} \frac{E}{E^{new}} f(\nu)$ .

Using the 2D criterion for blunt V-notches to calculate  $\mathcal{G}_c$ , we compute  $\mathcal{G}_c$  by [7, 42]:

$$\mathcal{G}_c(E^{new}) = \frac{A_{1C}^2 \cdot \Delta H_{11}^{new}(\mu_0) \cdot \rho^{2\alpha_1}}{\ell_0},$$

where  $A_{1C}, \mu_0, \ell_0, \rho$  are independent of  $E$ , and  $\Delta H_{11}^{new} = \Delta H_{11} \frac{E}{E^{new}} \frac{1-(\nu^{new})^2}{1-\nu^2}$ .  $A_{1C}$  is the 2D SIF at fracture of the experimental specimen with a sharp V-notch under mode I loading,  $\rho$  is the radius at the blunt notch tip,  $\mu_0$  is a function of  $\sigma_{\theta\theta}^{(1)} = \frac{\sigma_c}{A_{1C} \cdot \rho^{\alpha_1 - 1}}$ , and  $\ell_0 = \mu_0 \cdot \rho$ . We therefore obtain  $\mathcal{G}_c(E^{new}) = \mathcal{G}_c(E) \frac{E}{E^{new}}$ .

The same relation is obtained using Leguillon's criterion for a sharp V-notches [7]  $\mathcal{G}_c(E^{new}) = K^{new}(\omega) \cdot \left(\frac{A_{1C}}{\sigma_c^{2\alpha_1 - 1}}\right)^{\frac{1}{1-\alpha_1}} = K(\omega) \times \frac{E}{E^{new}} \frac{1-(\nu^{new})^2}{1-\nu^2} \times \left(\frac{A_{1C}}{\sigma_c^{2\alpha_1 - 1}}\right)^{\frac{1}{1-\alpha_1}}$ .  $A_{1C}, \sigma_c$  are independent on  $E$ , and again  $\mathcal{G}_c(E^{new}) = \mathcal{G}_c(E) \frac{E}{E^{new}}$ . Therefore, we computed  $\mathcal{G}_c$ , for the three materials with different  $E$ s.

## Appendix B. Experimental results: Failure origins, orientations, and failure loads for PMMA, Graphite and MACOR

Tables B.11-B.13 present detailed measurements of the forces to fracture for the three materials used in the experiments - commercial PMMA, Graphite and MACOR.

Tables B.15-B.21 present detailed measurements of the crack origins location and orientations. In the Cartesian coordinate representation, the V-notch edge coincides with the  $z$  axis, and  $z = 0$  is the point of intersection between the edge and the free surface at the back face of the specimen, with respect to its placement in the testing machine during the experiment.

In the blue light scan the measured specimens were always the *right* half of the broken bar specimen, in terms of its position in the machine during the 4PB test.

*Failure loads*

Detailed results of the force to fracture for specimens with notch height of  $6\text{ mm}$  are presented in Table B.11. and for notch height  $4\text{ mm}$ , in Table B.12.



specimen geometry	specimen number	failure load $N$	Average failure load $N$
$\gamma = 0^\circ$	1	928.5	922
	2	858.5	
	3	948.1	
	4	953.9	
$\gamma = 30^\circ$	11	1181.8	1213
	12	1276.2	
	13	1227.2	
	14	1168.2	
$\gamma = 45^\circ$	21	1560.8	1604
	22	1707.5	
	23	1627.7	
	24	1520.8	

Table B.11: Failure load in PMMA specimens, notch height  $h = 6\text{ mm}$ .

specimen geometry	specimen number	failure load $N$	Average failure load $N$
$\gamma = 0^\circ$	5	1137.1	1213
	6	1271.3	
	7	1230.7	
$\gamma = 30^\circ$	15	1572.4	1565
	16	1522.5	
	17	1598.9	
$\gamma = 45^\circ$	25	2001.3	2018
	26	2067.6	
	27	1984	

Table B.12: Failure load in PMMA specimens, notch height  $h = 4\text{ mm}$ .

Experimental results for Graphite and MACOR are presented in Tables B.13-B.14.

specimen geometry:	specimen number	failure load $N$	Average failure load $N$
$\gamma = 0^\circ$	1	668	668
$\gamma = 30^\circ$	3	865	846
	4	817	
	5	873	
	6	856	
	7	819	
$\gamma = 45^\circ$	8	1040	1028
	9	1025	
	10	1040	
	11	1031	
	12	1005	

Table B.13: Failure load in Graphite specimens, notch height  $h = 6 \text{ mm}$ .

specimen geometry:	specimen number	failure load $N$	Average failure load $N$
$\gamma = 0^\circ$	1	1013	996
	2	1100	
	3	936	
	4	939	
$\gamma = 30^\circ$	5	1346	1290
	6	1399	
	7	1325	
	8	1107	
$\gamma = 45^\circ$	9	1467	1489
	10	1445	
	11	1532	
	12	1512	

Table B.14: Failure load in MACOR specimens, notch height  $h = 6 \text{ mm}$ .

*Crack initiation locations and angles measurements*

specimen geometry (number)	Fracture origin location $z$ mm	Fracture origin angles	
		$\alpha$ [°]	$\theta^*$ [°]
$\gamma = 0^\circ$ (3)	uniform front	0	1
$\gamma = 30^\circ$ (11)	4	-22.5	-25.8
	5	-6.5	-10.4
	6.5	-12.8	-15.8
	8.5	5.1	21.5
	9.1	4	20.5
	10.1	-5.8	17.6
$\gamma = 30^\circ$ (12)	4.7	-23.9	-19.3
	6.2	-0.8	-1.39
	8.6	-7.9	-23.1
	9.6	-9	-5.1
$\gamma = 30^\circ$ (13)	4.5	-5.2	-15.7
	5.7	2.7	7.4
	6.8	26.8	25.2
	7.1	13.9	11.3
	7.6	3.2	13.3
	9.3	7.6	25.9
	10	0.9	21.6
$\gamma = 30^\circ$ (14)	3.9	-19.9	-22.8
	4.7	5.1	-13
	5.4	2.3	-12.6
	6.2	0.3	-3.1
	7	-2.2	9.6
	8.6	-0.3	8.9
	9.8	-10.1	-0.2

Table B.15: Crack initiation plane's angles for a PMMA specimens, notch height  $h = 6$  mm

specimen geometry (number)	Fracture origin location $z$ <i>mm</i>	Fracture origin angles	
		$\alpha$ [ $^\circ$ ]	$\theta^*$ [ $^\circ$ ]
$\gamma = 45^\circ$ (21)	12	-40.8	1.3
$\gamma = 45^\circ$ (22)	2.8	-40.3	-14.5
	3.4	-34	-5.4
$\gamma = 45^\circ$ (23)	2.8	-43	-12.4
$\gamma = 45^\circ$ (24)	4.3	-18.7	-17.1

Table B.16: PMMA - continued

For notch heights of 4 *mm*, angle measurements are available from the profilometer only.

We used an optical profilometer for PMMA specimens with a single origin. It is based on a scanning white light interferometry method (manufactured by Zygo, USA, 1998), with a  $\times 50$  magnification lens, producing 3-D pictures approximately 250  $\mu m$  over 290  $\mu m$  in size. The difficulty is the need to perform a coordinate transformation from profilometer's system (which is picture dependent), to the coordinate system in Figure 2, so that  $(\alpha, \theta^*)$  could be determined. Measurements taken for specimens with  $\gamma = 45^\circ$  are presented in Table B.17 (single origin). The crack origin is marked by an arrow.

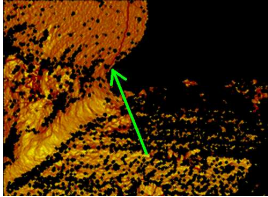
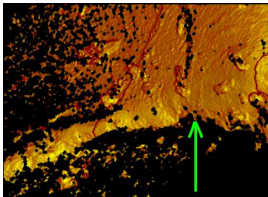
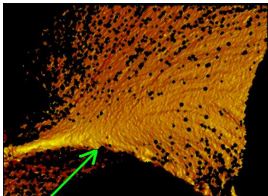
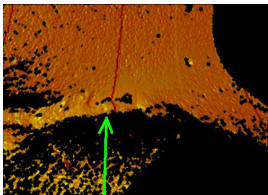
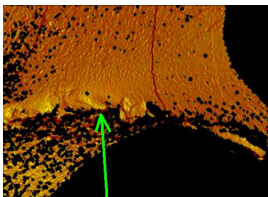
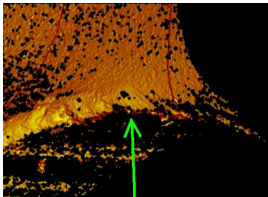
Specimen notation (number)	The crack origin profilometer view ( $\times 50$ magnification)	Fracture origin angles ( $\alpha, \theta^*$ ) [ $^\circ$ ]	$z$ mm
6mm45deg (21)		( $-30.4, -6$ )	12
6mm45deg (22)		( $-33.2, -13.6$ )	3.4
6mm45deg (23)		( $-31.3, -20.5$ )	2.8
4mm45deg (25)		( $-33.6, -3.6$ )	9.7
4mm45deg (26)		( $-33, -3.9$ )	7
4mm45deg (27)		( $-34.6, -5.7$ )	10.3

Table B.17: Crack initiation plane's angles for a V-notch with  $\gamma = 45^\circ$

The failure initiation angles in Table B.17 for each of the geometries are close:  $-30.4^\circ \leq \alpha \leq -39.8^\circ$ ,  $-20.5^\circ \leq \theta^* \leq -6^\circ$  for  $h = 6mm$ ,  $-5.7^\circ \leq \theta^* \leq -3.6^\circ$  for  $h = 4mm$  and  $8.9^\circ \leq \theta^* \leq 17.6^\circ$  for  $h = 2mm$ . An error estimation is of about  $\pm 5^\circ$ . This method is inefficient, and may not be implemented on specimens that have more than one crack origin. Therefore, most of the spatial angles measurements were done using the blue light scan. The angle measurements obtained by both methods (profilometer and blue light scan) can be compared only for PMMA specimens of the 6mm45deg geometry (No. 21-23), for which the profilometer results overestimate  $\alpha$  by less than  $12^\circ$  and underestimate  $\theta^*$  by less than  $8^\circ$  compared with the blue light scan.

specimen geometry (number)	Fracture origin location $z$ <i>mm</i>	Fracture origin angles	
		$\alpha$ [°]	$\theta^*$ [°]
$\gamma = 0^\circ$ (1)	0.5	-2.6	5.5
	1	0.4	-1.5
	1.4	-1.7	2.1
	2	3.2	3.4
	2.8	-5	5.2
	3.7	0.8	1.9
	4.5	-1.2	3.3
	5.3	-3.5	3.9
	6.2	5.7	2
	7.6	-4.2	-1.8
	8	-2.6	2.4
	8.7	-3.7	0.5
9.6	-0.3	-5	
$\gamma = 30^\circ$ (3)	0.6	-18.3	-22.5
	3.2	-15.1	-8.2
	4	-12.2	-10.3
	4.6	1.6	-5.1
	6.6	-9.8	-3.7
	7.9	-22.7	10.3
	9.1	-12.1	7.8
	9.9	-16.6	14.1
$\gamma = 30^\circ$ (4)	2.7	0.5	-16
	3.6	-3.6	-8
	4.6	-1.5	-6
	5.1	-5.5	-4.4
	6	-10.5	-5.2
	6.7	-13.5	-6.7
	7.7	-3.1	10
	8.9	-0.6	0.1
	10.4	-4.8	13.5
$\gamma = 30^\circ$ (5)	1.9	-3.1	-13.3
	2.6	-7.1	-15.9
	3.8	-5.5	-20.4
	4.9	-7.3	-7.7
	5.6	10.7	-12.4
	6.6	0.4	10.5
	7.7	-2.9	9.8
	8.8	-7.3	11.3
	9.6	-15.6	4.8
	10.4	-6.1	18.3

Table B.18: Crack initiation plane's angles for a Graphite specimens, notch height  $h = 6$  *mm*.

specimen geometry (number)	Fracture origin location $z$ mm	Fracture origin angles	
		$\alpha$ [°]	$\theta^*$ [°]
$\gamma = 30^\circ$ (6)	1.5	-1	-10.3
	2.2	-0.5	-18.8
	4.8	-14.5	-2.3
	5.8	-12	-1
	7.7	-12.4	2.7
	9	-2.9	12.9
	11	-10.9	22.2
$\gamma = 45^\circ$ (8)	3	-18	-0.4
	4	-9	-4.5
	5.7	-16.1	-17.1
	6.4	-14.1	-4.1
	7.5	-8.1	0.8
	9.8	-1.6	2
	11.2	-14.2	27.8
	12.2	-18.1	5.6
$\gamma = 45^\circ$ (9)	3.3	0.4	-6.5
	3.9	0.1	-1.8
	4.7	1	-0.7
	6.1	-6.9	3.8
	7.2	-6.9	14.8
	8.7	-6.2	9
	9.8	-22.1	7.7
	11	-10.2	-8.3
	11.7	-8	9.7
	12.6	0.5	19.6
	13.2	-0.7	8.9

Table B.19: Graphite - continued



specimen geometry (number)	Fracture origin location $z$ <i>mm</i>	Fracture origin angles	
		$\alpha$ [ $^\circ$ ]	$\theta^*$ [ $^\circ$ ]
$\gamma = 45^\circ$ (10)	1	-10.8	-42.6
	2.5	1.8	-32.2
	3.3	-7.9	-26
	4.1	-7.4	-20.2
	5.5	-9.1	-5.3
	6.7	-4.3	6.2
	7.5	-13.3	7.8
	8.3	-6.8	13.6
	8.8	-10.1	4.15
	11.2	-3.1	22.5
12.1	-16.8	35.3	
$\gamma = 45^\circ$ (11)	1.3	-21.5	-34.8
	2.6	-6.6	1.9
	3.5	-0.5	-6.2
	5.2	-16.6	13.9
	6.2	-11.3	8.5
	7.1	-16.7	14.3
	9.1	-4	11
	10.4	-10.1	27.6
	12.2	-3.9	17.7

Table B.20: Graphite - continued

specimen geometry (number)	Fracture origin location $z$ <i>mm</i>	Fracture origin angles	
		$\alpha$ [ $^\circ$ ]	$\theta^*$ [ $^\circ$ ]
$\gamma = 0^\circ$ (2)	1.6	6.2	-4.3
	3.5	-0.3	-15.5
	4.6	-2.2	-11.6
	5.5	2.1	-15
	6.7	-3.1	-8.6
	7.9	-2.7	-7.7
	8.9	-4.1	-4.3
	9.5	-1.8	-5.4
$\gamma = 30^\circ$ (5)	0.9	-11.7	-6.5
	1.9	-32.5	-20.8
	2.8	-22.6	4.2
	4.3	-25.3	9.2
	5.9	-12.5	-5
	7.1	-2.5	-12.7
	8	-10.5	5.2
	8.9	-6	8.7
	10.4	-19	1.6
$\gamma = 30^\circ$ (6)	1	-35	-46.5
	1.8	-18.3	-42.8
	2.5	-19.2	-23
	4.4	-15.7	-33.1
	5	-10	-18.3
	5.8	-15.4	-8.1
	6.7	-17.2	-26
	7.9	-41.3	-14.2
	8.7	-32	5
	10.5	-14.2	5.2
$\gamma = 30^\circ$ (7)	1.9	-28.6	-37.4
	2.7	7.3	-27.8
	3.9	4.7	-18.7
	5	-16	-27
	5.9	-23.3	11.2
	6.6	-9.5	6.2
	7.3	-20.4	0.4
	8	-12.1	-6.3
	8.8	-27	1.4
	9.6	-15.5	5

Table B.21: Crack initiation plane's angles for a MACOR specimens, notch height  $h = 6$  *mm*

specimen geometry (number)	Fracture origin location $z$ mm	Fracture origin angles	
		$\alpha$ [°]	$\theta^*$ [°]
$\gamma = 30^\circ$ (8)	0.6	-16.9	-9.3
	2.1	-16.8	-20.7
	3.5	-28.1	-21.2
	4.3	-9	7.5
	5.5	-6.2	0.5
	7.4	-22.6	-19
	8.2	-32.3	-2.8
	9.4	-10.8	12.4
$\gamma = 45^\circ$ (9)	10.2	-17.7	-7.2
	11.1	-21.1	-2.2
	12	-18.9	5.4
$\gamma = 45^\circ$ (10)	6.8	-5.1	-28.6
	7.6	-3.22	-18.1
	8.2	-20.8	-18.4
	9	-9.7	-17.1
	9.7	-27.6	-6.3
	11.4	-40.6	3
	12.8	-43.8	35.4
$\gamma = 45^\circ$ (11)	7.5	-21.9	-20
	8.4	-9.3	-6.6
	9	-9	-25.7
	9.8	-30.8	-10.4
	11.2	-30.2	1.3
	12	-26.1	-4.1
	12.5	-16.4	28.7
$\gamma = 45^\circ$ (12)	4.6	-27	-29.3
	5.5	-24.1	-20.5
	6.3	-24.8	1.3
	7.2	-11.1	10
	8.5	-7.8	1.8
	9.5	-31.6	7
	12.1	-14.2	4.4
	13	-40	22.4

Table B.22: MACOR continued

## Appendix C. Polynomial approximations of the GESIFs $A_i(z)$ for the specimens used in experiments

The GESIFs were computed using p-FEMs for the specimens used in our experiments. The following notations are used for the specimens

	$\gamma = 0^\circ$	$\gamma = 30^\circ$	$\gamma = 45^\circ$
$h = 4mm$	<i>4h0deg</i>	<i>4h30deg</i>	<i>4h45deg</i>
$h = 6mm$	<i>6h0deg</i>	<i>6h30deg</i>	<i>6h45deg</i>

Table C.23: Specimens notation.

The GESIFs  $A_i(z)$  along the V-notch edge were extracted by the QDFM [34]. The polynomials that represent the GESIFs are presented in Table C.24, for the average failure load on PMMA experiments.  $A_i(z)$  depend linearly on the force, so their values for any other load may be easily obtained, for the given geometries. The  $A_i(z)$  do not depend on material properties, so for the given geometries they apply to all materials used.

specimen	$A_1(z)$	$A_2(z)$	$A_3(z)$	at force of N
4h0deg	$-0.000184z^6 + 0.0055z^5$ $-0.069z^4 + 0.46z^3$ $-1.7676z^2 + 3.8726z$ $+19.5456$	0	0	1213
6h0deg	$-0.00018z^6 + 0.0054z^5$ $-0.06788z^4 + 0.4552z^3$ $-1.78z^2 + 4.0625z$ $+18.8749$	0	0	922
4h30deg	$-0.0000463z^6 + 0.0016z^5$ $-0.024z^4 + 0.197755z^3$ $-z^2 + 3.12z + 20.047$	$-3.84 \cdot 10^{-10}z^6 - 0.0003266z^5$ $+0.009428z^4 - 0.116755z^3$ $+0.7652z^2 - 3.19285z$ $+7.0194$	$-0.00002824z^6 + 0.0009784z^5$ $-0.014221z^4 + 0.111z^3$ $-0.53894z^2 + 1.72288z$ $-17.2226$	1565
6h30deg	$0.0000717z^6 - 0.00224z^5$ $+0.022z^4 - 0.0461z^3$ $-0.481z^2 + 2.9638z$ $+19.8462$	$-0.0001443z^6 + 0.004474z^5$ $-0.05z^4 + 0.2196z^3$ $-0.10873z^2 - 2.2893z$ $+7.6281$	$-0.0000219z^6 + 0.0007583z^5$ $-0.011z^4 + 0.086z^3$ $-0.41772z^2 + 1.33537z$ $-13.3489$	1213
4h45deg	$-7.86 \cdot 10^{-6}z^6 + 0.0003336z^5$ $-0.00643z^4 + 0.070765z^3$ $-0.5217z^2 + 2.5253z$ $+18.3964$	$1.616 \cdot 10^{-8}z^6 - 0.0001543z^5$ $+0.00544z^4 - 0.0848z^3$ $+0.71z^2 - 3.71314z$ $+9.83072$	$-0.0000556z^6 + 0.000236z^5$ $-0.00404z^4 + 0.035466z^3$ $-0.19625z^2 + 0.804757z$ $-23.978$	2018
6h45deg	$-2.517 \cdot 10^{-6}z^6 + 0.000107z^5$ $-0.00251z^4 + 0.03541z^3$ $-0.387z^2 + 2.6434z$ $+17.7341$	$-2.673 \cdot 10^{-8}z^6 - 0.0001264z^5$ $+0.0045z^4 - 0.06945z^3$ $+0.5741z^2 - 3.426z$ $+11.0881$	$-6.98 \cdot 10^{-6}z^6 + 0.000296z^5$ $-0.004925z^4 + 0.0405z^3$ $-0.20213z^2 + 0.786648z$ $-23.473$	1604

Table C.24: GESIFs  $A_i(z)$  for each specimen geometry, at PMMA failure load ( $z$  in mm, and GESIF in  $\text{MPa} \times \text{mm}^{1-\alpha_i}$ .)